

Synoptic And Dynamical Analysis Of Cold Air Outbreaks Over California Central Valley

By

Rui Zhang

2016

Table of Contents

Abstract

Part I Synoptic analysis

- 1. Introduction**
- 2. Data and methods**
- 3. Results**
- 4. Discussion and conclusion**

References

Part II Dynamical analysis

- 1. Introduction**
- 2. Data and methods**
- 3. Results**
- 4. Discussion and conclusion**

References

Acknowledgements

Appendix A

Appendix B

Abstract

The large scale meteorological patterns (LSMPs) associated with the cold air outbreaks (CAOs) over the California Central Valley (CCV) at onset have a strong warm ridge over the Bering Sea and western Alaska, another ridge over the Southeastern US, and a cold trough in between. We show the synoptic properties of how these LSMPs develop. A previously unheralded feature (strong surface pressure in the Gulf of Alaska) is key to the development of unusual warmth over Alaska and flow of unusual cold southeastward and then westward to the Pacific Northwest and California to create the CAOs. Three dimensional trajectory analysis and lag-lead composites with bootstrap resampling significance of temperature and mass fields describe the synoptic evolution.

A variety of tools reveal the dynamics of the LSMPs evolution. Temperature equation analysis identifies regions of local change due mainly to advection versus diabatic effects while tracing the path of the CAO air mass. The three-dimensional temperature structure and motion provide insight into how the strong anomalous high pressure develops in the Gulf of Alaska. Though quasi-geostrophic potential vorticity shows the variability between different CAO events prior to onset, all events have the trough-ridge-trough pattern of QGPV over Alaskan region-western coast-southeastern US at onset or on day -1. Small amplitude wave activity flux (WAF) shows largest amplitudes on the south sides of the LSMP features in the mass field beginning nearly a week in advance of the CAO reaching California. Finite amplitude local wave activity (LWA) tracks the growth of a large LWA center over the Alaskan region that broadens

longitudinally splitting off an LWA center that migrates over western Canada into the western US. Tropopause level divergent wind fields hint at a tropical connection but mainly encourage the westward migration of the cold air mass into California in the last days before onset.

Part I Synoptic analysis

1. Introduction

Cold air outbreaks (CAOs), a type of temperature extreme, have created multi-billion dollar losses in the state of California. Especially hard hit have been agricultural operations in the California Central Valley (CCV). Due to the large societal and economic consequences of the CAOs, work has been done to investigate CAOs in different regions of the world. Some of studies focus on the performance of model simulation and statistical analysis of CAOs (Whan and Zwiers 2016; Whan et al 2016), while other studies emphasize the interaction between the low frequency modes and the synoptic features associated with the extreme temperature events (Konrad 1998; Westby and Black 2015).

In addition, Grotjahn and Faure (2008) applied a compositing technique to identify the key parts of the continental-scale Large Scale Meteorological Patterns (LSMPs) for extreme temperature events. They found that the hard freezes are associated with the ridge-trough-ridge pattern over Alaska region-western coast-southeastern US in both the geopotential height and thermal fields. However, as pointed out in Grotjahn et al (2015), current knowledge about the synoptics and dynamical mechanisms leading to the associated LSMPs is incomplete.

The definition of the CAOs in the present study is quite different from that of hard freezes in Grotjahn and Faure (2008). Surface minimum temperature anomalies at multiple stations in the CCV plus 700hPa temperature anomaly at KOAK are used by us to isolate events, while they use total field of minimum temperature and subsequent maximum temperature from only one station (Executive Airport station) in Sacramento to identify events. However, the

purposes of including the 700hPa temperature anomaly at KOAK in the present study and the subsequent maximum temperature in Grotjahn and Faure (2008) are the same, selecting for situations where strong cold air advection dominates rather than strong near-surface radiational cooling.

The first part of this work doesn't involve diagnostic analysis of model outputs as what was included in Colle and Mass (1995) and doesn't use many statistical tools to establish a statistical model. The only statistical tool we use to identify the significance of the LSMPs is the bootstrap test analysis. This work centers around the three dimensional synoptic structures associated with CAOs consisting of large scale meteorological features at surface level (i.e. temperature anomalies, sea level pressure and surface winds), synoptic patterns of geopotential height anomaly (500hPa and 1000hPa) and temperature anomaly (700hPa), vertical synoptic structures of winds and temperature anomalies shown in pressure-longitude or pressure-latitude cross sections, and backwards trajectories analysis. In short, we are trying to tell a complete and compelling synoptic story about CAOs in the CCV.

The first part of this present study focuses on the synoptic analysis of CAOs in boreal winter. Data and methods used to isolate and investigate the extreme temperature events are described in the next section. This is followed in section 3 by an examination of synoptic structures and the evolutions of the LSMPs associated with the CAOs. Conclusions and discussions are presented in section 4.

2. Data and Methods

2.1 Data

The CAO events are isolated from daily surface minimum temperature values at 17 National Climatic Data Center (NCDC) stations located across the California Central Valley. The 700hPa temperature at Oakland radiosonde station is also used to exclude CAO events mainly induced by strong near-surface radiational cooling in favor of events with extreme cold in much of the lower troposphere. The events favored will have strong cold air advection in addition to nocturnal radiational cooling.

The synoptic analyses are based on National Centers for Environment Prediction-National Center for Atmospheric Research reanalysis 1 dataset (NNRA1) (Kalnay et al. 1996). The spatial and temporal resolutions are respectively 2.5x2.5 degrees and 4 times daily. The data used include 62 boreal winters (Dec-Jan-Feb) from 1951 to 2013. The European Centre for Medium-Range Weather Forecasts (ECMWF) interim reanalysis product (ERA-interim; Dee et al. 2011; <http://apps.ecmwf.int/datasets/data/interim-full-daily/>), with resolution 0.25x0.25 degrees, is used to cross-check the three dimensional backwards trajectories.

2.2 Methods

2.2.1 Event isolation and ranking

The procedure for isolating CAO events is as follows.

- 1.) The long term daily mean (LTDM) of daily surface minimum temperature (T_{mn}) at each station is calculated over 63 years (1951-2013). That is, for example, daily surface minimum temperature of Jan. 1st of each year is added up together and then the sum is divided by the number (63) of years to get the raw LTDM for Jan. 1st. By this way, we obtain the raw LTDM of T_{mn} for each day of the whole year (365 days). To avoid unreasonable temperature jumps between two adjacent days, we apply Fourier analysis to the raw LTDM separately for each station. Before Fourier analysis, we shift the time period used to start from 1 August and

end with 31 July. The purpose of this rearrangement is to place any discontinuous jump of Fourier analysis at these time boundaries in the summer, far removed from the winter period considered here. Next, the first five harmonics, which sum to be closest to the original LTDM, are used as the smoothed, final LTDM to calculate the anomaly of daily surface minimum temperature for each day of each winter season. Each winter includes 90 days, from Dec 1st through Feb 28th. The same technique is used by Lee and Grotjahn (2016) to define the LTDM, but for summer months.

2.) Long term daily mean standard deviation (LTDMSD) of daily surface minimum temperature over the winter season is calculated for each station with the smoothed LTDM. For each station, the arithmetic mean of LTDMSD of T_{mn} over winter season is calculated to obtain a representative LTDM standard deviation for each station. Using this winter-long average is reasonable based upon plots of the LTDMSD of T_{mn} over winter season for each station; we find that all of the 17 lines of LTDMSD are pretty flat (not shown here). Then the anomaly of daily surface minimum temperature for each day obtained in step 1.) is normalized by the mean LTDMSD of each corresponding station. The result is a normalized daily surface minimum temperature (hereafter NmT_{mn}) for each day; NmT_{mn} is used to isolate CAO events.

3.) The dates when the coldest 5% NmT_{mn} values occur for each station are selected. We retain those dates that are common to at least 9 stations. Then events are identified when there are at least two consecutive retained days in a row.

4.) Meanwhile, 700hPa temperature anomaly at KOAK is required to be less than -0.5 °C on the onset day. 32 CAO events are obtained by this procedure. We rank these 32 events from lowest to highest sum of NmT_{mn} values (Table 1 in Appendix A). This sum only uses stations meeting the 5% NmT_{mn} criterion.

Hartmann and Wendler (2005) investigated the significance of the 1976/1977 climate shift, which refers to that the Pacific Decadal Oscillation (PDO) index shifted from dominantly negative values for the 25-year time period (1951-75) to dominantly positive values for the period 1977-2001, for the climatology of Alaska. They found that the time means of several meteorology variables (i.e. temperature, wind, sea level pressure, geopotential height) are distinctly different between the two time periods above. As we use a composite technique in the present study, we prefer to group the CAOs into two groups (before and after 1979) simply based on the onset date of the events to avoid the impact of the complexity of this climate shift on the synoptic analysis here. Thus, only the strong 10 CAO events after 1979 (Table 1) are studied here. Other events before 1979, which can be a comparison to this study, might be investigated later.

Event No.	Onset date
1	19901221
2	19890205
3	20070112
4	19981221
5	20120116
6	20110227
7	20020130
8	20091208
9	20130113
10	19870116

Table 1: Onset date of the strong 10 CAOs 1979-2013

2.2.2 Backwards trajectories

Backwards trajectories have been successfully used by Lee and Grotjahn (2016) to help classify and uncover the dynamical mechanisms of extreme summertime heat events. Here we only intend to track, backwards in time, the paths of the cold air that reaches the lower troposphere above the CCV at onset of CAOs, rather than classifying the events. Below is the 8-step procedure to calculate a backwards trajectory from NNRA1.

Step 1: Choose the original grid point $(\theta_1, \varphi_1, P_1)$ in the CCV to trace back in time. Note that θ_1, φ_1 and P_1 are respectively the longitude, latitude and pressure. Step 2: Obtain the wind field (u_1, v_1, w_1) at the original grid point $(\theta_1, \varphi_1, P_1)$ at -0 Hour, which is 1200 UTC on the onset day. Step 3: Calculate the first guess position $(\theta_2, \varphi_2, P_2)$ at -6 Hour (6 hours earlier) by the following equations

$$\theta_2 = \theta_1 - \frac{u_1 \times \Delta t}{a} \frac{180}{\pi} \times \frac{1}{2} \left(\frac{1}{\cos \varphi_1} + \frac{1}{\cos \varphi_2} \right)$$

$$\varphi_2 = \varphi_1 - \frac{v_1 \times \Delta t}{a} \frac{180}{\pi}$$

$$P_2 = P_1 - w_1 \times \Delta t,$$

where a is the radius of the Earth and $\Delta t = 6 \text{ hour} = 21600 \text{ Sec}$. Step 4: Obtain the wind field (u_2, v_2, w_2) at the first guess position $(\theta_2, \varphi_2, P_2)$ by interpolation which is described as follows.

(i) Horizontal interpolations at 8 vertical levels are calculated by method of cubic spline interpolation under tension. The 8 levels are 1000hPa, 925hPa, 850hPa, 700hPa, 600hPa, 500hPa, 400hPa, 300hPa. (ii) Then vertical interpolation is calculated by cubic spline interpolation. Step 5: Calculate the final location $(\theta_0, \varphi_0, P_0)$ at -6 Hour by adjusted wind (u, v, w)

$$u = (u_1 + u_2)/2, v = (v_1 + v_2)/2, w = (w_1 + w_2)/2$$

$$\theta_0 = \theta_1 - \frac{u \times \Delta t}{a} \frac{180}{\pi} \times \frac{1}{2} \left(\frac{1}{\cos \varphi_1} + \frac{1}{\cos \varphi_0} \right)$$

$$\varphi_0 = \varphi_1 - \frac{v \times \Delta t}{a} \frac{180}{\pi}$$

$$P_0 = P_1 - w \times \Delta t .$$

Step 6: Treat this point $(\theta_0, \varphi_0, P_0)$ as the first guess position to iterate Step 4 and Step 5 20 times so that the final position converges in the following sense.

$$\Delta\theta_0 < 0.0001 \text{ degree}, \Delta\varphi_0 < 0.0001 \text{ degree}, \Delta P_0 < 0.01 \text{ hPa}$$

Step 7: The six steps above are applied using the following six grid points at 700hPa as the original position, (122W, 39N), (122W, 40N), (121W, 37N), (121W, 38N), (120W, 36N), (120W, 37N). At first, 25 time steps (6h interval) are traced back. Then we measure the confidence limit of our trajectory method for each event as follows. (i) (121W, 38N) is chosen as the mid-grid point. Among all the other five grid points, (122W, 40N) is used to calculate the farthest distance with the great circle formula. Denote this farthest distance as *dimax*. The value of two times *dimax* (563km) is used as the threshold to measure our confidence limit. (ii) The mean of the six trajectories is calculated and then we only include time steps where all six trajectories are not further than the above threshold 563km from the mean trajectory. By this way, we identify the time steps over which we have confidence in the trajectories for each event.

The process may limit the trace back as 16 rather than 25 time steps. The word trajectory hereafter in this study would indicate the mean trajectory of the six trajectories for each event.

Step 8: Note that in every step of the computation, surface pressure is interpolated to check if the particle's location is below ground. When trajectory pressure is greater than surface pressure, trajectory pressure is replaced by surface pressure. Also, the wind field is replaced by the wind at

the surface. We also tested calculating trajectories of four strongest events from ERA-interim data and found no appreciable difference between NNR1 and ERA-interim results (not shown here).

2.2.3 Lead-lag composite

A composite technique is used for either the anomaly or total fields at fixed times prior to the event onset to understand the evolution of the LSMPs. Consistency between the 10 events is measured by the sign count (Grotjahn 2011). A sign count is calculated by counting the number of events with the same sign of the anomaly at each grid point. In other words, the number of events with positive sign at a grid point is subtracted by the number of events with negative sign at that grid point. Thus, a sign count of 10 here means all events at that grid point have positive anomaly; absolute values of sign count greater than 3 mean at least 7 of the 10 events have the same sign of anomaly at that location. Besides sign count, a statistic method named bootstrap is used to measure the significance of the LSMPs (Grotjahn and Faure 2008). Bootstrap is a non-parametric way of comparing a given ensemble average with randomly-drawn ensembles at the same location. Bootstrap values here compare the value of ensemble mean to the distribution of values from the randomly-drawn ensembles and expresses it in terms of a percentage on the range of randomly-drawn ensemble values.

3. Results

3.1 Surface structures

As shown in figure 3.1.1, there is a noticeable cold air anomaly over Alaska 5 days prior to the onset, which strengthens gradually as it moves into the CCV at onset. Meanwhile, a warm

air anomaly develops over the Alaskan area and attains its maximum (12°C) at onset. In contrast, the warm air anomaly in the eastern US tends to be more stationary. We observe that different events have different growth rates of temperature anomaly prior to onset (i.e. figure 1 to 3 in Appendix), but they tend to be in phase at onset with the area of color enlarging (figure 3.1.1). In detail, 8 of the 10 events have warmth extending across the Bering sea with the time of the initial presence of this warmth varying between events from five days to two days before the onset; 7 of the 10 events have warmth across the Arctic Canada by the onset, but both the spatial coverage

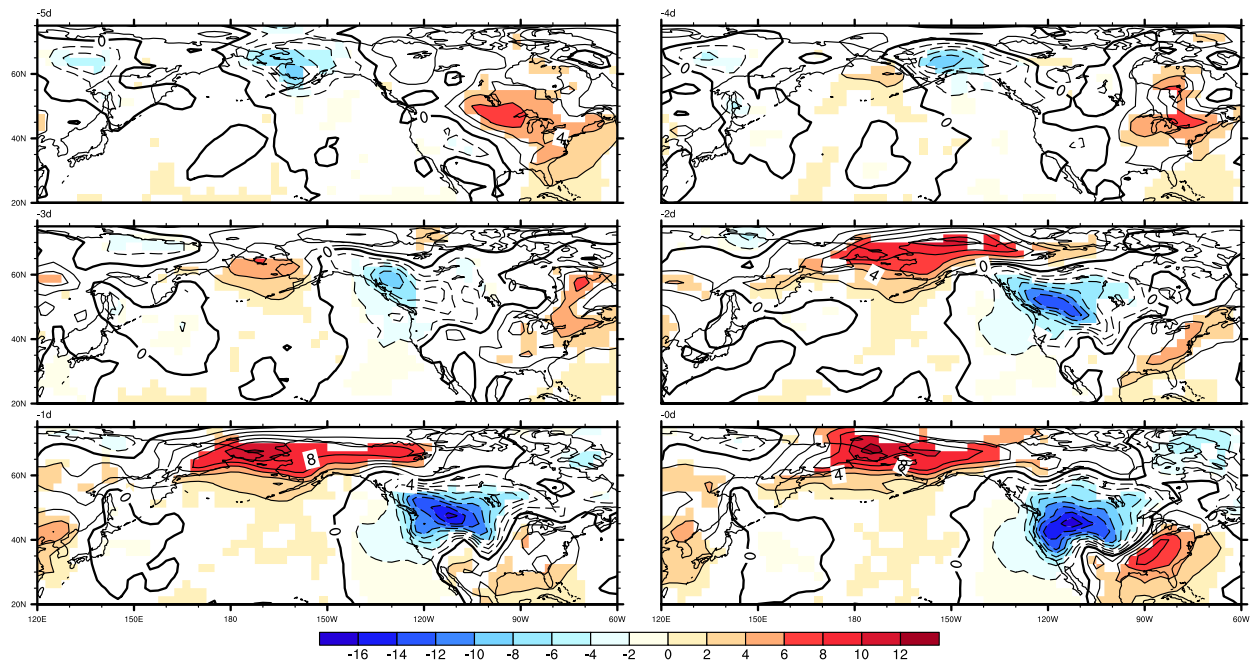


Fig 3.1.1 Composites of the 10 CAOs for surface temperature anomaly at sigma 0.995 for days before onset. The label ‘-Nd’ in the upper left corner of each map denotes N days prior to the onset (all times are 12 UTC). Grid points where absolute values of sign count are greater than 3 are shown in shaded color. The contour interval is 2°C. A significant temperature ridge-trough-ridge pattern develops over Alaska-Western Coast-Southeast US.

and the strength of this warm anomaly vary greatly between events; 8 of the 10 events have a cold anomaly in the Alaskan region five days before the onset, however, the time of this cold anomaly arriving in the northern part of CCV varies from day -4 to the onset (due to the space

limit, only three figures as a representative sample are shown in Appendix A, figure 1-3). Day -2 is the first day that most events (7 of 10) have the ridge-trough-ridge (Alaskan region-western coast-southeastern US) pattern in place with the number of events which have the similar LSMPs increasing to 10 at onset. In contrast, only one event has this LSMPs in place at day -3. It is the feature of different events tending to be more in phase as the onset is approached that explains the large growth rate ($-4^{\circ}\text{C}/\text{day}$) of the cold anomalies in two consecutive days (day -2 and day -1) and the noticeable enlarging of area of cold anomalies at onset (figure 3.1.1). Similarly, the warm anomalies over the Alaskan region have large growth rate ($4^{\circ}\text{C}/\text{day}$) at day -2 and its largest area expansion of warm anomalies at the same time (figure 3.1.1).

The cold temperature anomaly over the eastern Gulf of Alaska (figure 3.1.1) is crucial for the unusual sea level pressure in that region (figure 3.1.2). It is interesting to note that the cold anomalies are mostly confined to land area with the minimum decreasing from -8°C to -16°C over day -4 to the onset, however, the cold anomalies over the ocean are mostly between -2°C to -4°C during the same period.

An unusual high of sea level pressure, which is higher than 1030hPa, sits in the Gulf of Alaska, just off the western coast (figure 3.1.2) for several days prior to onset. This sea level pressure high does not move as much as the high of sea level pressure over the cold interior of western North America. Also, the 1000hPa geopotential height anomaly field in figure 3.2.2 emphasizes this anomalous high of sea level pressure in the Gulf of Alaska with a maximum of anomalous height 200m in the same region.

As the warm anomalies over the Alaskan region with an expansion over the Bering Sea develop over day -3 to the onset (figure 3.1.1), the strong low pressure centering the eastern

coast of Asia expands northeastward across the Bering Sea to reach the western boundary of Alaska during the same period (figure 3.1.2).

Over day -4 to the onset, the center of the high of sea level pressure over the cold interior of western North America (figure 3.1.2) matches well with that of the cold anomalies moving into CCV (figure 3.1.1). Although the cold anomalies over the eastern Gulf of Alaska is relatively small, its position is quite consistent with that of the unusual high sea level pressure in the Gulf of Alaska.

On day -4 and day -3, the strong northwestward sea level pressure gradient on the southeast part of the high of sea level pressure over the continent implies the northwesterly wind over the western Canada (figure 3.1.3) which drives the cold anomalies southeastward towards the CCV (figure 3.1.1). On day -2 and day -1, the strong northeastward sea level pressure gradient near the western coast of US (figure 3.1.2) is consistent with the easterly components of the surface wind near (120W, 50N) (figure 3.1.3), which drive the cold air westward into the CCV.

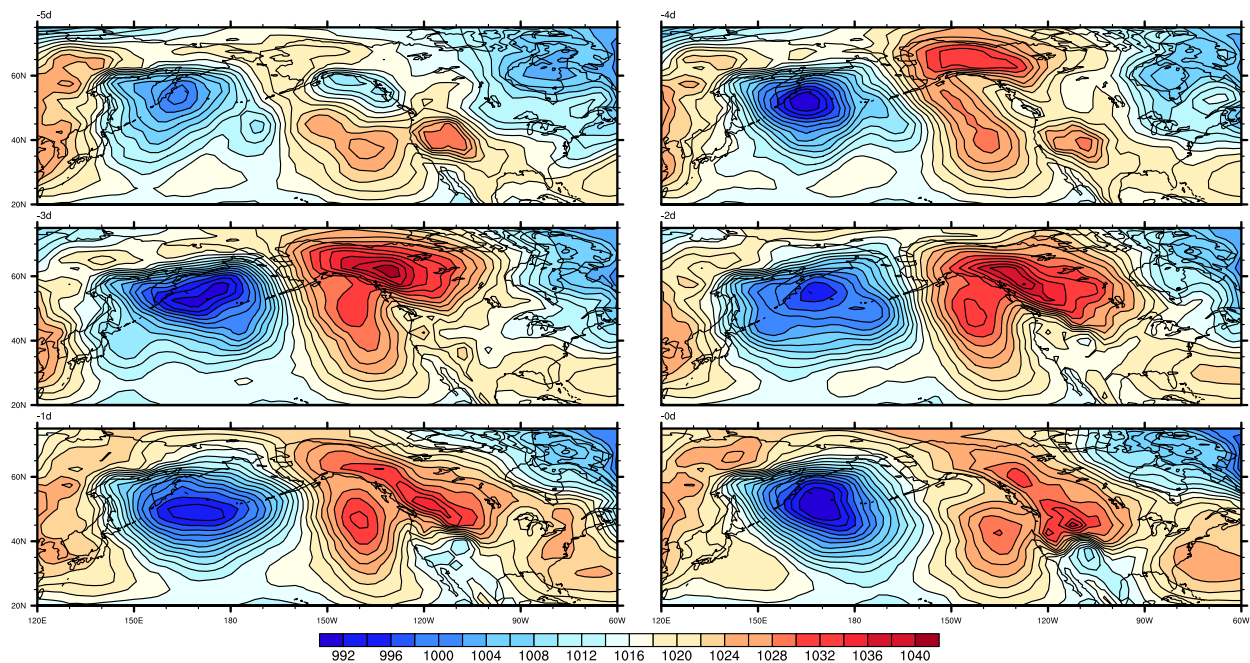


Fig 3.1.2 Composites of the 10 CAOs for sea level pressure. The string ‘-Nd’ in the upper left corner of each map denotes N days prior to the onset (all times are 12 UTC). Contour interval is 2hPa.

The southerly winds in between the low and high of sea level pressure in the central North Pacific, which is strongest just south of Bering Sea on day -3 and day -2 (figure 3.1.3), help build the temperature ridge over Alaskan region in figure 3.1.1 by warm air advection. These southerly winds almost always parallel with the sea level pressure contour.

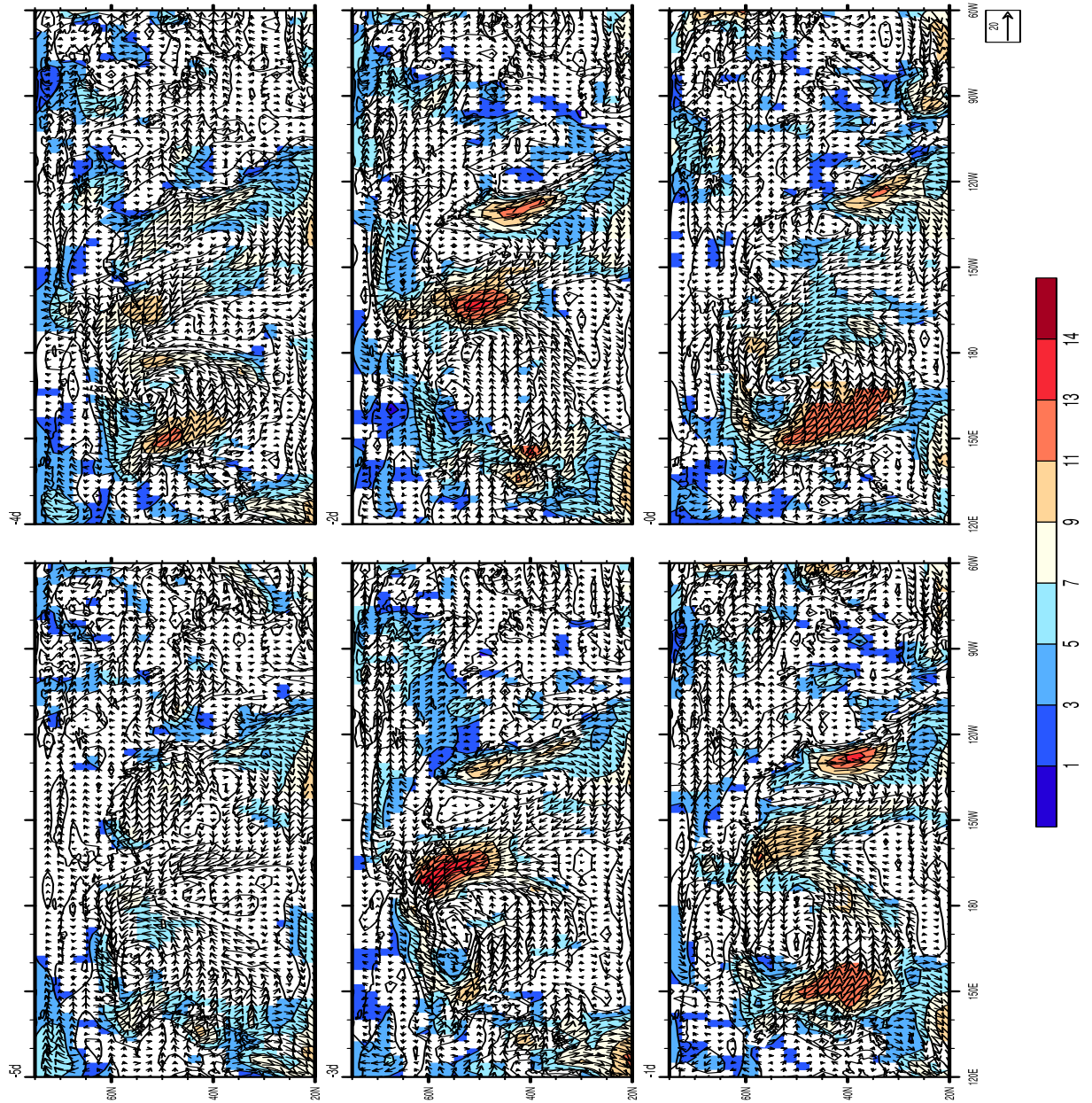


Fig 3.1.3 Composites of the 10 CAOs for surface wind at sigma 0.995. This figure is rotated 90° to the left to enlarge it. The string ‘-Nd’ in the upper left corner of each map denotes N days prior to the onset (all times are 12 UTC). Contours indicate the speed of the wind. The contour interval is 2m/s. Meridional wind is used to calculate the sign count. Grid points where absolute values of sign count are greater than 3 are shown in shaded color.

However, it is another story in or near land area. Day -5, westerly wind crossing the sea level pressure contour (figure 3.1.2) is seen over Alaska, carrying the cold air anomaly eastward

(figure 3.1.1). On day -4 and day -3, the strong surface flow along or offshore that parallels the Canadian coast (corresponding to the unusual high of sea level pressure in the Gulf of Alaska in figure 3.1.2) and the northwesterly wind east of the Canadian Rockies (which is due to the pressure gradient force generated by the high of sea level pressure over the Alaskan region in figure 3.1.2), bring the cold air anomaly southeastward along the western coast of North America (figure 3.1.1). On day -2 and day -1, accompanied with the movement of the core of the sea level pressure high over the continent towards the CCV (figure 3.1.2), there is noticeable easterly or northeasterly wind which crosses the Rockies and moves the core of cold air anomaly westward (figure 3.1.1). Meanwhile, there is evident northerly winds near or off the western coast of US (strongest on day -1 just off the western coast) which continue to bring more cold air into the California (figure 3.1.1).

3.2 Geopotential height and temperature anomaly

The ridge-trough-ridge pattern (Gulf of Alaska-Western Coast-Southeastern US) of 500hPa geopotential height anomaly, which is similar to the LSMPs shown in Grotjahn and Faure (2008), becomes significant from 3 days prior to the onset (figure 3.2.3). This highly significant pattern becomes stronger as the time is closer to the onset and has large swaths with statistical significance values greater than the 99.5% threshold. Parts of the pattern move as onset approaches: the Alaskan ridge and the trough, while the southeastern US ridge is more stationary as noted for the surface temperature. Similar movements of features of LSMPs with high significance are found in anomalous temperature field (figure 3.2.1). Also, the geopotential height anomaly field has an equivalent barotropic feature (i.e. the patterns in the lower and upper levels share high similarity as seen in figure 3.2.2, figures 4 and 5 in Appendix A).

The areas that are highly significant (larger than 99.5%) become larger as time is closer to the onset, especially the trough over western coast and the ridge over southeastern US (figure 3.2.1). Although individual event tends to have smaller area of high significance than that of the composite, most events have at least one or two parts of the LSMPs passing significance test. Also, the central extreme value of the western coast trough decreases from -5°C to -13°C as this

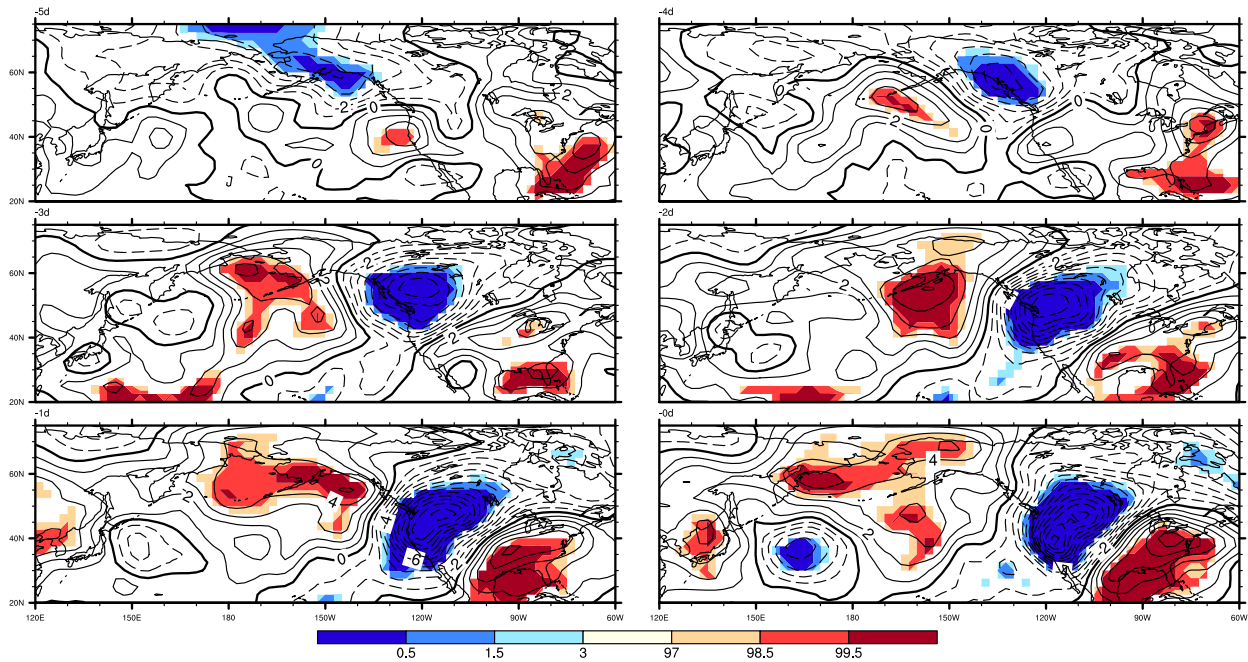


Fig 3.2.1 Composites of the 10 CAOs for anomalous temperature at 700hPa (contours), shadings indicate the significant areas which pass the Bootstrap test. Negative values have dashed contours while positive values use solid contours. Contour interval is 1°C . The string ‘-Nd’ in the upper left corner of each map denotes N days prior to the onset (all times are 12 UTC).

trough moves into the CCV over day -5 to the onset. As stated for surface temperature anomaly in section 3.1, the feature of different events tending to be more in phase as time is closer to the onset makes the composite temperature anomalies both statistically more significant and colder at onset than time prior to the onset. For example, the central extreme values of the western coast trough are smaller than -12°C in the CCV for all events on the onset, however, it varies from -10°C to 8°C in the CCV on day -5 between events (not shown here). Some events have an already

strong trough moving into the CCV; some have a preexist trough in place which becomes stronger gradually towards onset; some are a mix of the two previous cases.

The 1000hPa anomalous geopotential height (figure 3.2.2) has a core of high in the Gulf of Alaska, which matches well with the unusual sea level pressure high in the same region (figure 3.1.2). This unusual high extends to the western Canada, though it is not as strong as the part in the Gulf of Alaska. The trough at 1000hPa become noticeable on day -1 and is much weaker than the 500hPa trough (figure 3.2.3).

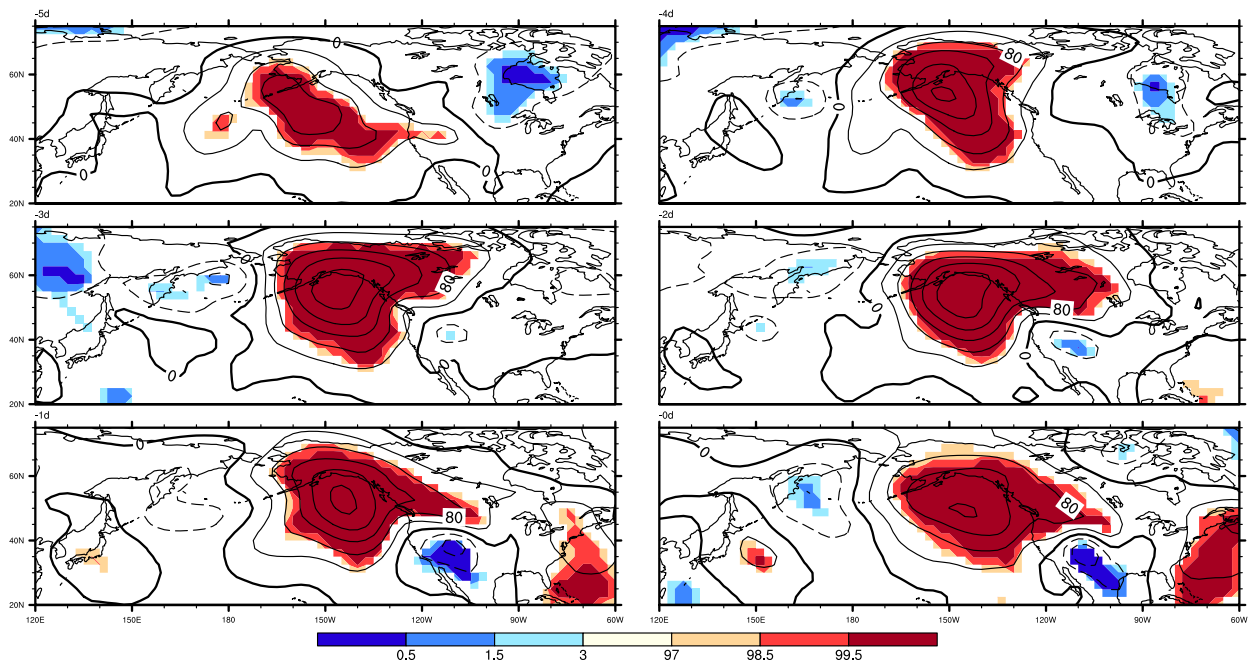


Fig 3.2.2 Same as figure 3.2.1, but for geopotential height anomaly at 1000hPa. Contour interval is 40m.

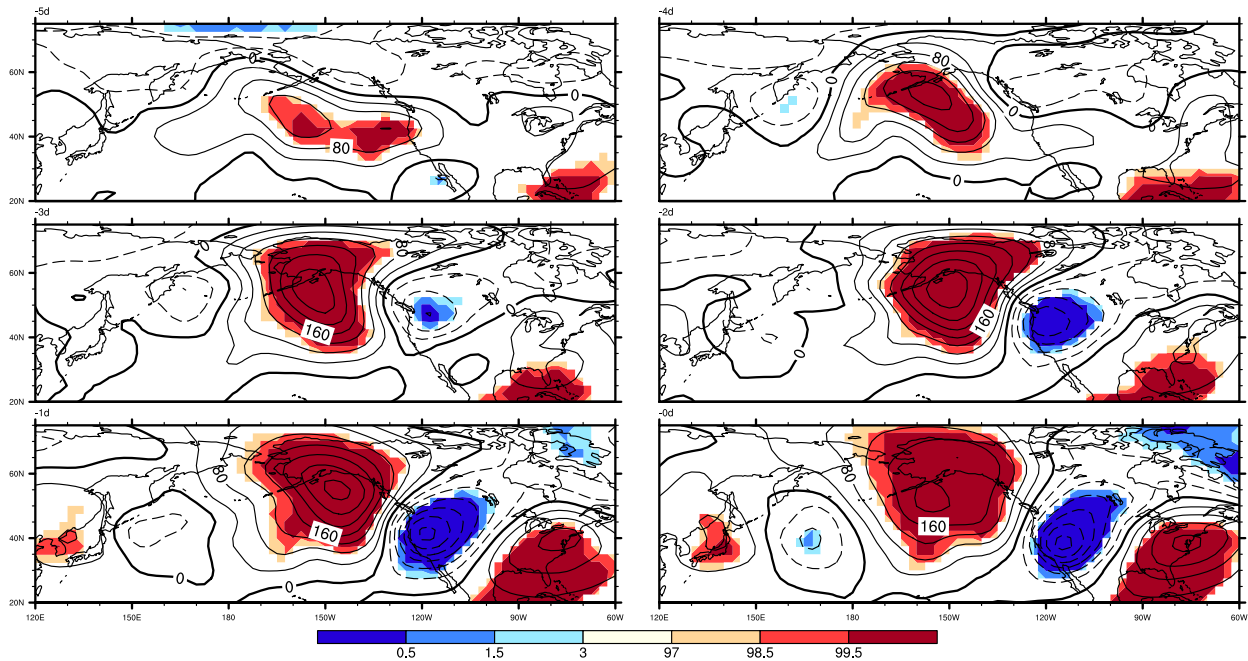


Fig 3.2.3 Same as figure 3.2.1, but for geopotential height anomaly at 500hPa. Contour interval is 40m.

The peak values of the geopotential height anomaly of both the Alaskan ridge and southeastern US ridge at 500hPa (figure 3.2.3) are much bigger than that of 1000hPa (figure 3.2.2) over day -3 to the onset (80m difference on day -2 and day -1), leading to an anomalous thicker layer over these two regions which is consistent with the anomalous higher temperature at 700hPa in the same regions (figure 3.2.1). The temperature trough over the western coast is consistent with the trough of the geopotential height field at these two levels in the same sense.

Both the areas of high significance (larger than 99.5%) and the peak values of the geopotential height anomalies of the LSMPs become larger as the time is approaching the onset (figure 3.2.3). As argued for temperature anomalies at 700hPa, the fact that different events with different moving rates tend to be more in phase at onset contributes to the formation of the above feature a lot. For example, the time of having the ridge-trough-ridge (Alaskan region-western coast-southeastern US) pattern in place varies from day -3 to the onset between events (not

shown here); the composite peak value of the southeastern ridge increases gradually from 40m to 160m over day -4 to the onset (figure 3.2.3) and 7 of the 10 events have its largest magnitude of the southeastern trough at onset.

3.3 Cross sections: temperature anomaly, meridional (zonal) wind, vertical wind

In this section, the three dimensional structure related to the CAOs will be shown with a series of cross-sections in the zonal and meridional planes. In all the pressure-longitude cross sections (figure 3.3.1-3.3.3), the rising happens primarily between the low in the western North Pacific and the high in the Gulf of Alaska of figure 3.1.2, consistent with the northward component of the surface winds in the central North Pacific (figure 3.1.3). The southerly wind and positive temperature anomaly in longitude range 180~150W of figures 3.3.1-3.3.3 imply warm air advection in almost the whole layer of 500hPa-1000hPa, which helps build the ridge over the Alaskan region and explains the barotropic feature seen in section 3.1. The warm advection is strongest at upper level on day -2 in all three pressure-longitude cross sections.

In figure 3.3.1 and figure 3.3.2, the sinking is mainly in the east part of the sea level pressure high over the Gulf of Alaska where there is also a cold air anomaly (shown in figure 3.1.1). In figure 3.3.1, this sinking becomes stronger and shifts eastward as the time is approaching the onset, which is consistent with the southeastward movement of the core of the sea level pressure high over the Gulf of Alaska (figure 3.1.2). However, this sinking in figure 3.3.2 is strongest on day -2 when the sea level pressure high over the Gulf of Alaska is strongest and centers around (140W, 50N). Consistently, as this sea level pressure high moves southward, there is no noticeable sinking in the same region on day -1 and the onset in figure 3.3.3.

Northerly wind (~east of 140W) is also found in the east part of the high over the Gulf of

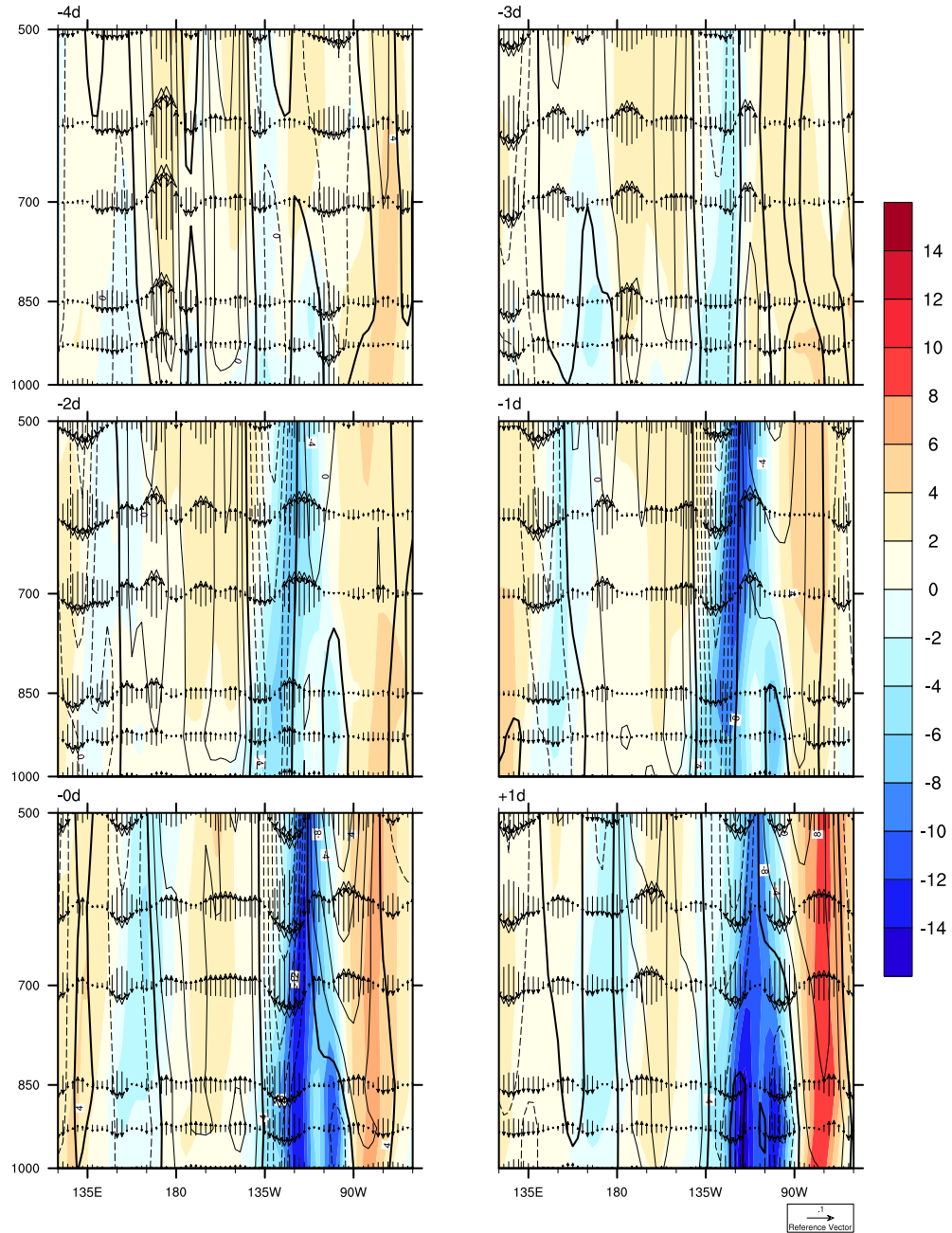


Fig 3.3.1 Pressure-Longitude cross section at 40N for composite of the 10 CAOs. Color indicates temperature anomaly with interval 2K. Meridional wind is shown in contour. Negative values have dashed contours while positive values use solid contours. Zero contours are indicated by darker solid lines. Contour interval is 4m/s. Vector denotes minus pressure velocity. The reference value for pressure velocity is 0.1 Pa/s. The string ‘-Nd’ (+Nd) in the upper left corner of each map denotes N days prior to (after) the onset (all times are 12 UTC). The northern part of the CCV is near ~120W longitude on these cross sections.

Alaska in both the lower and higher levels. This northerly wind is much stronger on day -1 than day -3 in all the pressure-longitude cross sections (figures 3.3.1-3.3.3), which is consistent with the strengthening of the ridge over Alaskan region (figure 3.2.3). The center of this northerly wind band also shifts eastward towards 120W (the position of the north part of the CCV) as the time is approaching the onset especially in figure 3.3.2 and figure 3.3.3. Those northerly winds are driving the cold air quickly down along the western coast which helps to sustain the cold air anomaly (seen in figure 3.1.1) and the upper air ridge (figure 3.2.3) also drives cold air southward above, so there is a thick layer of cold air that helps build the 500hPa trough.

As the center of the high of sea level pressure inland moves southeastward on day -1 and the onset, the notable northerly wind band extends to 90W at lower levels in figure 3.3.1. Over day -4 to day -1, the rising near 120W (figure 3.3.3, southeast of the core of the sea level pressure high over the continent) leads to the southeastward movement of this sea level pressure high (figure 3.1.2). As this sea level pressure high moves southeastward, there is also a noticeable southward shift of westerly wind band (figure 3.3.4), which gives way to the weak but important easterly wind band (between two darker zero contours, 40~50N over day -2 to the onset) through a considerable depth where the coldest anomalies are. In upper levels, the presence and the southward shift of this weak easterly wind band is also consistent with the strengthening and southward expansion of the notable geopotential height trough over the western coast over day -2 to the onset in figure 3.2.3. As commented in section 3.1 for figure 3.1.3, these easterly components of the winds are important for carrying the cold air westward into the CCV. It is of interest to notice that the vertical motion near 40N in figure 3.3.4 changes from rising to strong sinking over day -2 to the onset, which is consistent with the southeastward movement of both the sea level pressure high inland (figure 3.1.2) and the cold anomaly (figure 3.1.1).

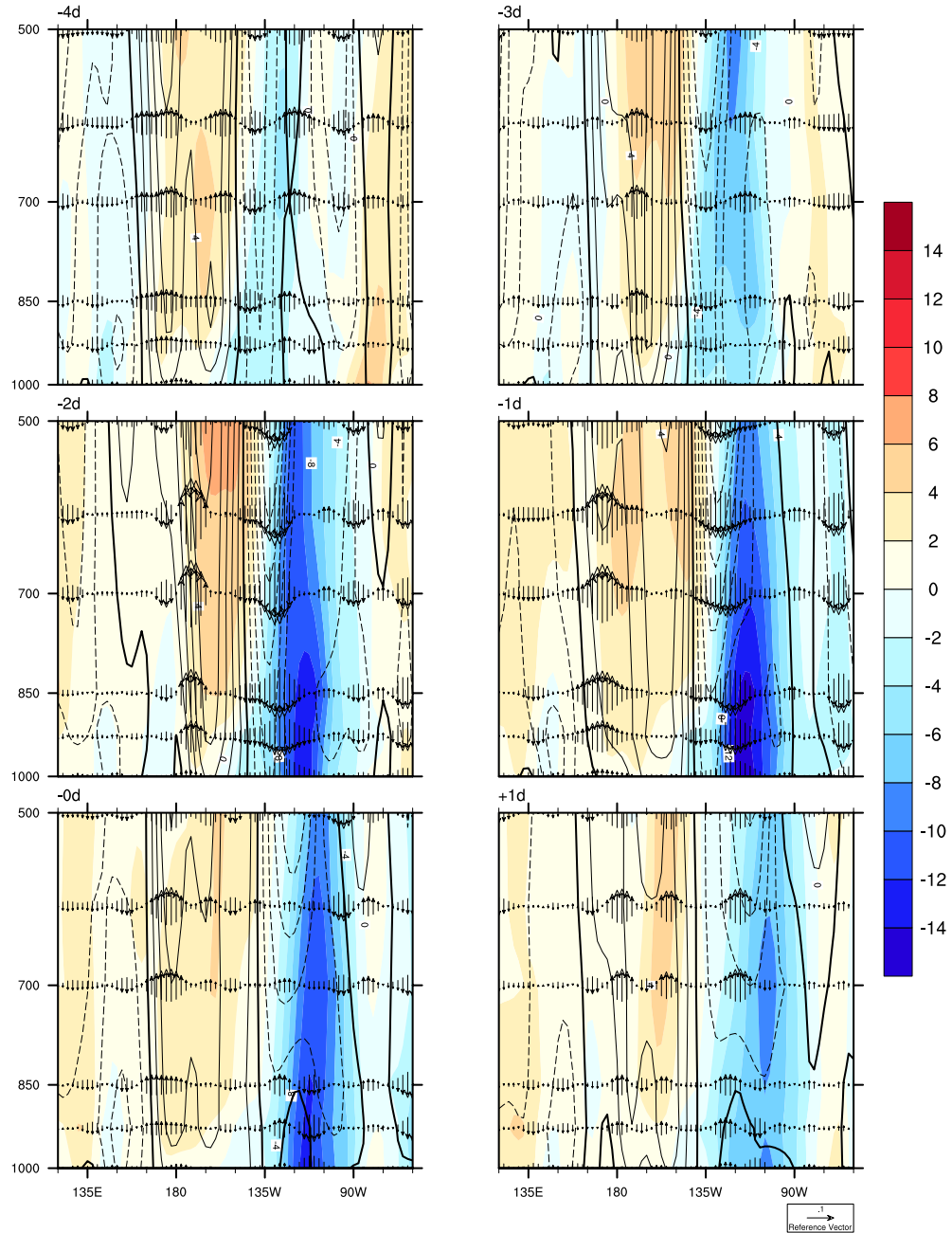


Fig 3.3.2 Same as figure 3.3.1, but at 50N.

In both figure 3.3.2 and 3.3.3 (about 135W~150W), there is a notable shallow cold air layer near the surface in the region of sea level pressure high (Gulf of Alaska) with warm air anomaly above. This warm anomaly above the cold anomaly explains the unusual feature that the ridge in the mid and upper troposphere is above the sea level pressure high.

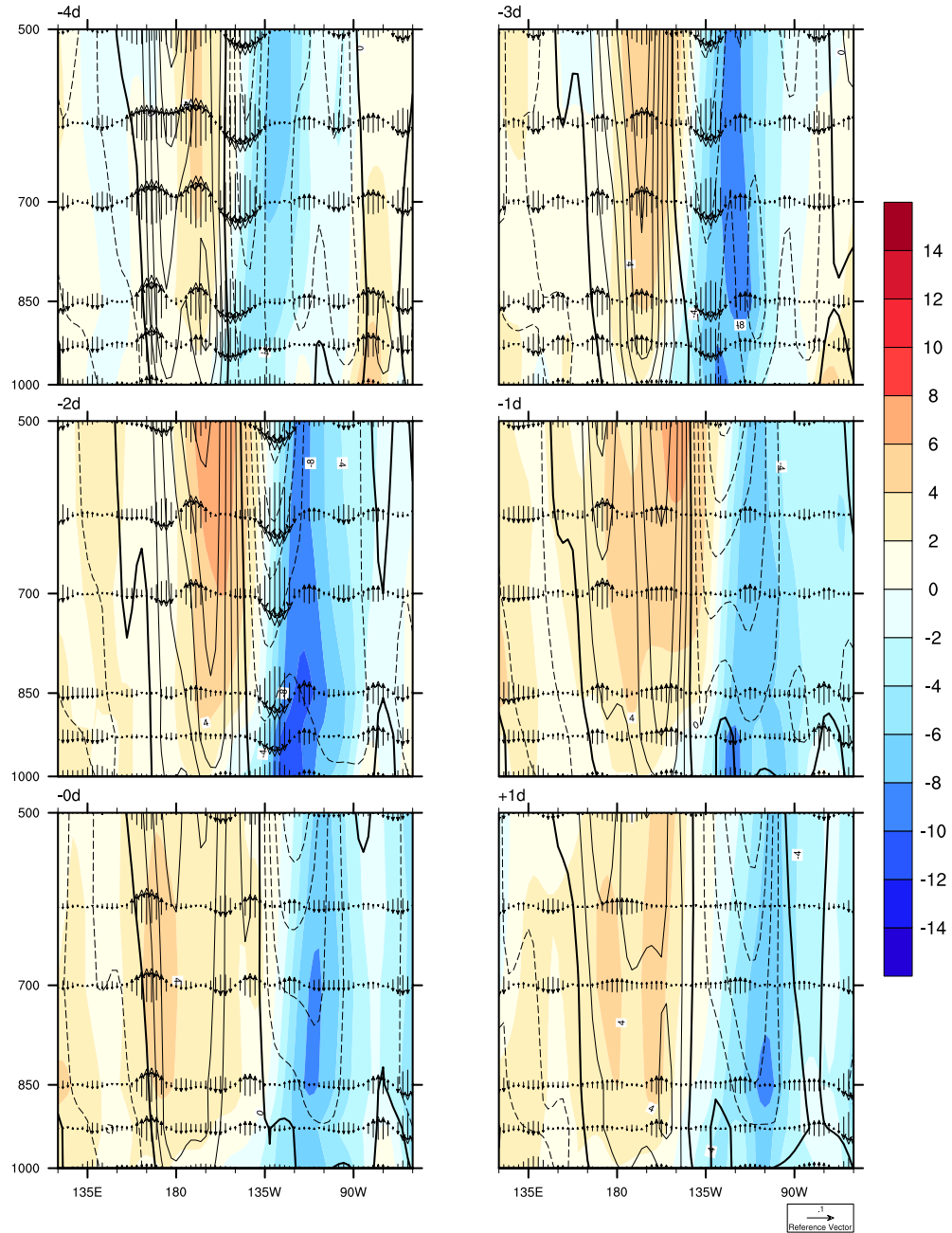


Fig 3.3.3 Same as figure 3.3.1, but at 55N.

Most of these synoptic properties associated with the CAOs in the CCV are quite large in spatial scale, much larger than the area of the CCV. In fact, the CAOs over the CCV affect a much larger region, especially to the north of the CCV (figure 3.1.1). Another two pressure-

longitude cross sections are shown in Appendix A (figures 6 and 7) with the hope of providing more synoptic information.

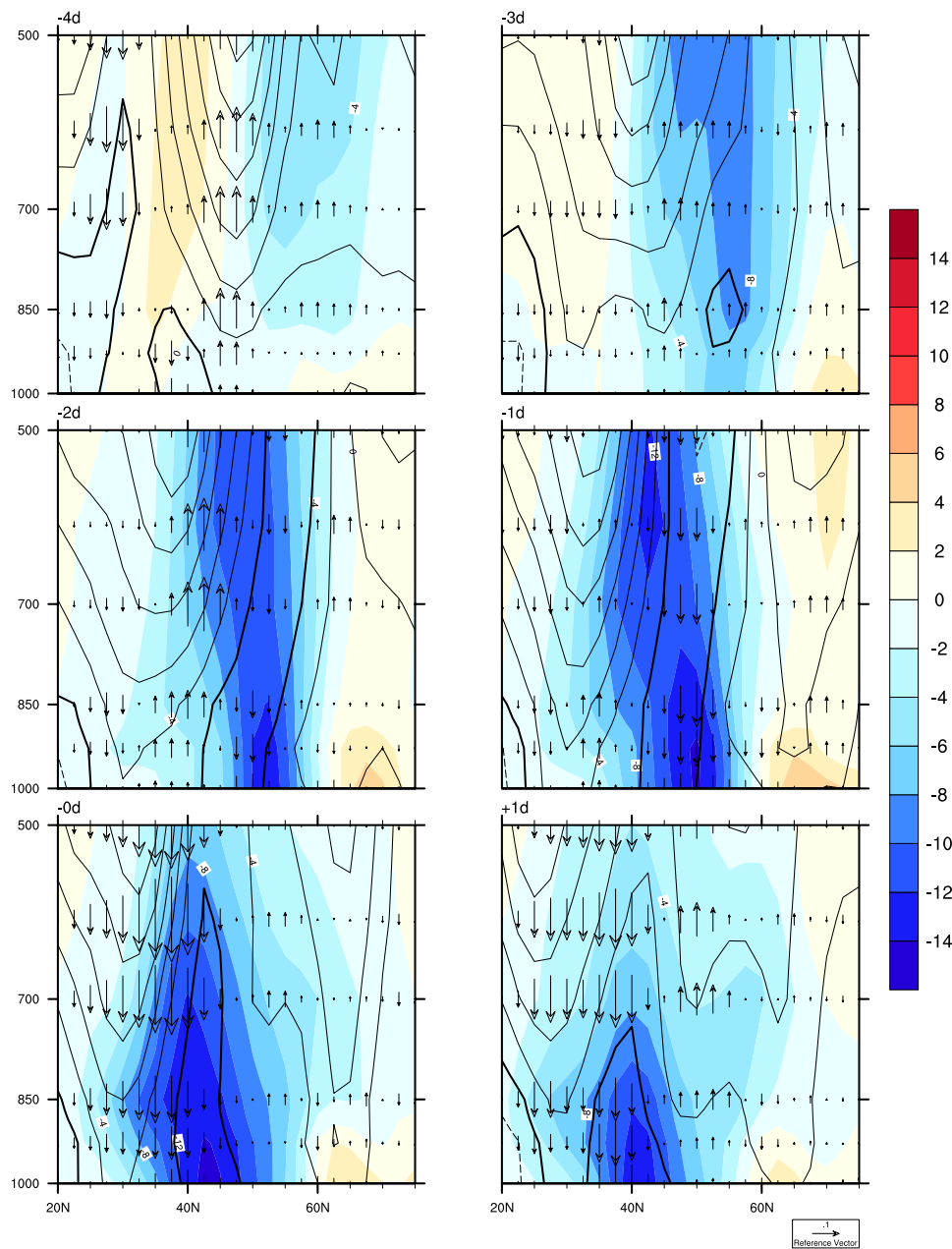


Fig 3.3.4 Pressure-Latitude cross section at 120W for composite of the 10 CAOs. Color indicates temperature anomaly with interval 2K. Zonal wind is shown in contour. Negative values have dashed contours while positive values use solid contours. Zero contours are indicated by darker solid lines. Contour interval is 4m/s. Vector denotes minus pressure velocity. The reference value for pressure velocity is 0.1 Pa/s. The string ‘-Nd’ (+Nd) in the upper left corner of each map denotes N days prior to (after) the onset (all times are 12 UTC). The CCV is approximately between 35 to 40N latitude on these panels.

3.4 Backwards trajectories

Figure 3.4.1 shows the mean trajectories (mean of trajectories from six grid points) for each of the 10 events. As stated above, these mean trajectories for each event go back in time only as long as all the members of the mean trajectory follow a path within a certain distance of the mean. Here, all the trajectories go back about 4 days.

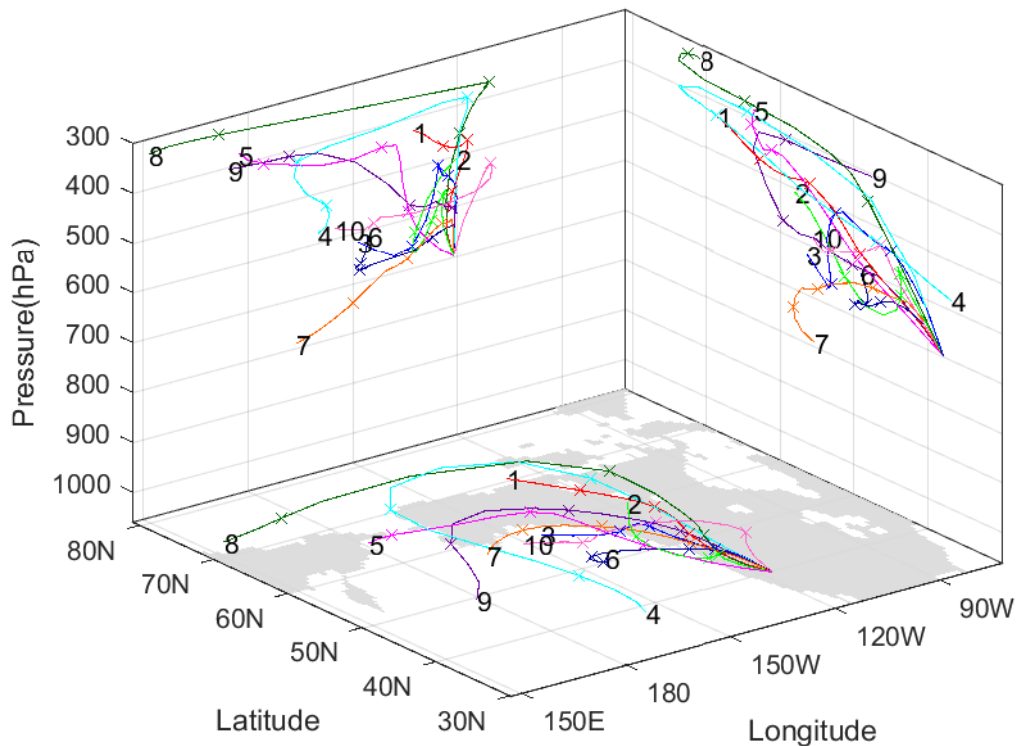
Near the onset, almost all events have trajectories coming down to the CCV from at least 10 degrees latitude north of the CCV with one path arriving from the east side of the Rockies. Prior to that, half of them move monotonically, steadily sinking while traveling southward from further north near or in the Polar region, although some events have a starting point in the Pacific and different events have different moving speeds. This southward movement is consistent with the movement of surface air temperature anomaly shown in figure 3.1.1 and the implied cold advection.

More than half of the 10 trajectories have an arc: first moving eastward then curving towards the south, which is consistent with the 500hPa ridge over the Alaskan region. About half of the 10 trajectories are along the coast though quite high up. So they are not modified much by marine interactions. We also find that the surface winds over the ocean are parallel to these trajectories and quite strong near the coast. While several trajectories are just onshore, one is over the ocean (number 5) but moves very quickly during the final 24 hours and is also at a high altitude. Thereby its modification by the ocean is limited. Three others (number 8, 1 and 10) have a path across the Rockies and avoid crossing the ocean.

Near the onset, all events show sinking although some of them rise a little bit before sinking. Only one event has a starting point lower than 700hPa. We also found sinking near the CCV in both the pressure-longitude cross section (figure 3.3.1, west of 120W) and pressure-

latitude cross section (figure 3.3.4, at or north of 40N on day -1 and the onset). In addition, the trajectories tend to have a higher consistency near the onset (day -1) than times prior to that time.

The trajectories that start at 850hPa (figure 8 in Appendix A) have much difference from that of 700hPa. Four trajectories (number 5, 3, 6, and 1) rise a lot while crossing the ocean. Only one trajectory (event 4) has an arc path as found in figure 3.4.1. About half of the 10 trajectories don't move very much compared with trajectories in figure 3.4.1. Despite of these differences of trajectories between two levels, several trajectories for 850hPa have a path along the coast as in figure 3.4.1. However, we have to mention that much of inland area of the western coast has a surface pressure smaller than 850hPa. So during our calculation of trajectories for 850hPa, surface pressure and the corresponding wind fields are used many times (see step 8 in section 2.2.2 for detail).



3.4.1 Backwards trajectories of the 10 CAOs with projections onto latitude-pressure, longitude-pressure, latitude-longitude planes trace back to about 4 days before the onset from 700hPa.

Different events are shown with different colors. Event numbers (Table 1) are marked at the end of each line. Every 24h is marked by a cross marker “x”. Gray area in the bottom plane indicates the land.

4. Discussion and conclusion

The unusual sea level pressure high in the Gulf of Alaska which is previously unheralded is crucial to the development of unusual warmth over Alaska and flow of unusual cold southeastward and then westward to the Pacific Northwest and California to create the CAOs. The cold anomaly in the Gulf of Alaska has smaller magnitude than the cold air minimum over North America. Though shallow and confined to the lowest portion of the atmosphere, the cold air over the Gulf of Alaska is denser than air over the sea to the west and creates the higher sea level pressure. The pattern and movement of the sea level pressure high over the continent are consistent with the movement of the cold anomalies at surface and the surface winds.

The highly significant LSMPs of temperature anomaly and geopotential height anomaly at onset have a strong warm ridge over the Bering Sea and western Alaska, another ridge over the Southeastern US, and a cold trough in between, which are consistent with the ones shown in Grotjahn and Faure (2008). The statistical significance and the central extreme values of the LSMPs become larger as the time approaches the onset due to the fact that different events tend to be more in phase as time is closer to the onset. Also, the evolutions of the geopotential height anomalies at 500hPa and 1000hPa and temperature anomalies at 700hPa are consistent in the sense that 700hPa temperature anomalies can be a proxy of the thickness of 1000hPa-500hPa surfaces. LSMPs are an equivalent barotropic, nearly-stationary wave train (ridge-trough-ridge) across the North Pacific and western North America. The North Pacific ridge expands northward in the composite and covers the whole Alaskan region with high significance (larger than 99.5%) on day -3. The highly significant ridge near the southeastern US attains its maximum near the

onset. The trough in between these two ridges develops on day -3 and continues to amplify towards the onset.

The meridional and zonal winds shown in cross sections help explain the evolution of the LSMP structures at various levels of the troposphere. The rising between the sea level pressure low in the western North Pacific and the high of sea level pressure in the Gulf of Alaska explains the northward component of the surface winds in the central North Pacific. This southerly wind and positive temperature anomaly in longitude range 180~150W of figures 3.3.1-3.3.3 imply warm air advection in almost the whole layer of 500hPa-1000hPa, which helps build the ridge over the Alaskan region and explains the barotropic feature seen in section 3.1. The sinking is mainly in the east part of the sea level pressure high over the Gulf of Alaska where there is also a cold air anomaly. The northerly winds near 120W (figures 3.3.2-3.3.3) are driving the cold air quickly down along the western coast which helps to sustain the cold air anomaly (seen in figure 3.1.1) and the upper air ridge (figure 3.2.3) also drives cold air southward above, so there is a thick layer of cold air that helps build the 500hPa trough. The presence and southward shift of the weak easterly wind band in a considerable depth in the pressure-latitude cross section (figure 3.3.4) shows the westward movement of cold air into the CCV. The warm anomaly above the shallow cold anomaly in figures 3.3.2 -3.3.3 explains the unusual feature that the ridge in the mid and upper troposphere is above the high of sea level pressure in the Gulf of Alaska.

Backwards trajectories are calculated to obtain an intuitive way to show the complex path followed by the cold air to reach the CCV. Trajectories based on a final location (12UTC at onset) of 700hPa over the CCV are chosen since using lower start elevations leads to encounters with surface topography. All the trajectories show southward motion and sinking during (at least) the last 24 hours (some trajectories much longer than that) as the air approaches the CCV. While

some trajectories pass over the continent during the 4 days shown, some pass near the North America coast even off shore. When doing so, the air parcels are above 700hPa elevation and unlikely to be modified by interactions with the ocean surface. There is quite a bit of variation between trajectories in terms of the speed and level from which the cold air reaches 700hPa above the CCV. Most of them come from the mid to upper troposphere, though there are some exceptions.

References

Colle B. A., and C. F. Mass, 1995: The structure and evolution of cold surges east of the Rocky Mountains. *Mon. Wea. Rev.*, 123, 2577–2610, doi:[10.1175/1520-0493\(1995\)123,2577:TSAEOC.2.0.CO;2](https://doi.org/10.1175/1520-0493(1995)123,2577:TSAEOC.2.0.CO;2).

Dee, D. P., and Coauthors, 2011: The ERA-Interim reanalysis: Configuration and performance of the data assimilation system. *Quart. J. Roy. Meteor. Soc.*, 137, 553–597, doi:[10.1002/qj.828](https://doi.org/10.1002/qj.828).

Grotjahn, R., 2011: Identifying extreme hottest days from large scale upper air data: A pilot scheme to find California Central Valley summertime maximum surface temperatures. *Climate Dyn.*, 37, 587–604, doi:[10.1007/s00382-011-0999-z](https://doi.org/10.1007/s00382-011-0999-z).

———, and G. Faure, 2008: Composite predictor maps of extraordinary weather events in the Sacramento, California, region. *Wea. Forecasting*, 23, 313–335, doi:[10.1175/2007WAF2006055.1](https://doi.org/10.1175/2007WAF2006055.1).

———, and Coauthors, 2015: North American extreme temperature events and related large-scale meteorological patterns: A review of statistical methods, dynamics, modeling, and trends. *Climate Dyn.*, 1–34, doi:[10.1007/s00382-015-2638-6](https://doi.org/10.1007/s00382-015-2638-6).

Hartmann, B., and G. Wendler, 2005: The significance of the 1976 Pacific climate shift in the climatology of Alaska, *J. Clim.*, 18, 4824–4839, doi:[10.1175/JCLI3532.1](https://doi.org/10.1175/JCLI3532.1).

Kalnay, E., and Coauthors, 1996: The NCEP/NCAR 40-Year Reanalysis Project. *Bull. Amer. Meteor. Soc.*, 77, 437–471, doi:[10.1175/1520-0477\(1996\)077,0437:TNYRP.2.0.CO;2](https://doi.org/10.1175/1520-0477(1996)077,0437:TNYRP.2.0.CO;2).

Konrad, C. E., II, 1998: Persistent planetary scale circulation patterns and their relationship with cold air outbreak activity over the eastern United States. *Int. J. Climatol.*, 18, 1209–1221, doi:[10.1002/\(SICI\)1097-0088\(199809\)18:11,1209::AID-JOC301.3.0.CO;2-K](https://doi.org/10.1002/(SICI)1097-0088(199809)18:11,1209::AID-JOC301.3.0.CO;2-K).

Lee, Y-Y. and R. Grotjahn, 2016: California Central Valley summer heat waves form two ways. *J. Clim.*, 29, 1201–1217, doi: [10.1175/JCLI-D-15-0270.1](https://doi.org/10.1175/JCLI-D-15-0270.1).

Westby, R. M., and R. X. Black, 2015: Development of Anomalous Temperature Regimes over the Southeastern United States: Synoptic Behavior and Role of Low-Frequency Modes. *Wea. Forecasting*, 30, 553-570, doi: [10.1175/WAF-D-14-00093.1](https://doi.org/10.1175/WAF-D-14-00093.1).

Whan, K., and F. W. Zwiers, 2016a: Evaluation of extreme rainfall and temperature over North America in CanRCM4 and CRCM5. *Climate Dyn.*, 46, 3821–3843, doi:[10.1007/s00382-015-2807-7](https://doi.org/10.1007/s00382-015-2807-7).

Whan, K., F. W. Zwiers and J. Sillmann, 2016: The influence of atmospheric blocking on extreme winter minimum temperatures in North America. *J. Atmos. Sci.*, 29, 4361-4381, doi: [10.1175/JCLI-D-15-0493.1](https://doi.org/10.1175/JCLI-D-15-0493.1).

Part II Dynamical analysis

1. Introduction

The first part of this study discusses the three dimensional synoptic structures of large scale meteorological patterns (LSMPs) associated with cold air outbreaks (CAOs) in the California Central Valley (CCV) and finds that the LSMPs at onset, which is consistent with that of Grotjahn and Faure (2008), have a strong warm ridge over the Bering Sea and western Alaska, another ridge over the Southeastern US, and a cold trough in between. Also, we find a previously unheralded feature (strong surface pressure in the Gulf of Alaska) which is key to the development of unusual warmth over Alaska and flow of unusual cold southeastward and then westward to the Pacific Northwest and California to create the CAOs. However, part I does not present a systematic study of the dynamical mechanisms of how the LSMPs develop, thereby motivating this work reported here.

Previous investigations about how the cold air outbreaks generate emphasize different aspects, i.e. the effects of topography (Colle and Mass, 1995), accompanying low or high frequency disturbances (Lau and Lau, 1984; Westby and Black, 2015). In detail, Colle and Mass (1995) emphasized the interaction of the evolving synoptic-scale flow with the Rocky Mountains and the sloping topography of the Great Plains. Temperature tendency equation and vorticity equation were used by them upon the model outputs to determine whether the advection or the topographic Rossby wave is the dominant process. In our study, temperature tendency equation is applied to reanalysis data, rather than model outputs, to find out the contributions to the local temperature change in the lower troposphere.

Small amplitude wave activity flux (WAF) developed by Takaya and Nakamura (2001) is used by us in the way similar to that of Bueh et al (2011) who found, by this method, that the

positive height anomaly associated with persistent low temperature over Southern China is maintained by incoming Rossby wave packets from central Siberia and by those from West Asia along the subtropical jet stream. Although it is argued sometimes that WAF is unable to describe the large magnitude of waves associated with extreme temperature events, we suspect that linear WAF provides us, at least, with a description of the linear part of the extreme temperature events. On the other hand, as argued in Takaya and Nakamura (2001), a stationary Rossby wave train emanating from a blocking ridge or an incoming one from upstream to the ridge should exhibit nonlinearity to a much lesser degree than the high-amplitude blocking ridge itself, and hence they may be suitable for applying small amplitude WAF.

Besides small amplitude WAF, we also use finite amplitude local wave activity developed by Huang and Nakamura (2016) to capture the evolution of the Alaskan ridge which is similar to a blocking and crucial to the occurrence of the CAOs in the CCV. Although energy balance of eddies associated with CAOs (i.e. conversion of available potential energy and kinetic energy shown in Lau and Lau 1984) is not included in this study, the temporal evolutions of dynamical diagnostic quantities such as small amplitude wave activity flux, finite amplitude wave activity and tropopause level divergent wind fields should provide the readers with the energy source from a different perspective. In addition, we also delineate the primary dynamical structures of LSMPs by presenting the evolution of quasi-geostrophic potential vorticity (QGVP) of individual event.

The second part of this study focuses on the dynamical mechanism of how the LSMPs develop. The next section describes the data and dynamical analysis methods used to analyze the events. For clarity and completeness, the procedure of event isolation and ranking in part I is

reiterated here. Main results are presented in the third section, which is followed by a brief conclusion and discussion in section 4.

2. Data and Methods

2.1 Data

The CAO events are isolated from daily surface minimum temperature values at 17 National Climatic Data Center (NCDC) stations located across the California Central Valley. The 700hPa temperature at Oakland radiosonde station is also used to exclude CAO events mainly induced by strong near-surface radiational cooling in favor of events with extreme cold in much of the lower troposphere. The events favored will have strong cold air advection in addition to nocturnal radiational cooling.

The dynamical analyses are based on National Centers for Environment Prediction-National Center for Atmospheric Research reanalysis 1 dataset (NNRA1) (Kalnay et al. 1996). The spatial and temporal resolutions are respectively 2.5x2.5 degrees and 4 times daily. The data used include 62 boreal winters (Dec-Jan-Feb) from 1951 to 2013.

2.2 Methods

2.2.1 Event isolation and ranking

The procedure for isolating CAO events is as follows.

1.) The long term daily mean (LTDM) of daily surface minimum temperature (T_{mn}) at each station is calculated over 63 years (1951-2013). That is, for example, daily surface minimum temperature of Jan. 1st of each year is added up together and then the sum is divided by the number (63) of years to get the raw LTDM for Jan. 1st. By this way, we obtain the raw LTDM of T_{mn} for each day of the whole year (365 days). To avoid unreasonable temperature

jumps between two adjacent days, we apply Fourier analysis to the raw LTDM separately for each station. Before Fourier analysis, we shift the time period used to start from 1 August and end with 31 July. The purpose of this rearrangement is to place any discontinuous jump of Fourier analysis at these time boundaries in the summer, far removed from the winter period considered here. Next, the first five harmonics, which sum to be closest to the original LTDM, are used as the smoothed, final LTDM to calculate the anomaly of daily surface minimum temperature for each day of each winter season. Each winter includes 90 days, from Dec 1st through Feb 28th. Same technique is used by Lee and Grotjahn (2016) to define the LTDM, but for summer months.

2.) Long term daily mean standard deviation (LTDMSD) of daily surface minimum temperature over the winter season is calculated for each station with the smoothed LTDM. For each station, the arithmetic mean of LTDMSD of T_{mn} over winter season is calculated to obtain a representative LTDM standard deviation for each station. Using this winter-long average is reasonable based upon plots of the LTDMSD of T_{mn} over winter season for each station; we find that all of the 17 lines of LTDMSD are pretty flat (not shown here). Then the anomaly of daily surface minimum temperature for each day obtained in step 1.) is normalized by the mean LTDMSD of each corresponding station. The result is a normalized daily surface minimum temperature (hereafter NmT_{mn}) for each day; NmT_{mn} is used to isolate CAO events.

3.) The dates when the coldest 5% NmT_{mn} values occur for each station are selected. We retain those dates that are common to at least 9 stations. Then events are identified when there are at least two consecutive retained days in a row.

4.) Meanwhile, 700hPa temperature anomaly at KOAK is required to be less than -0.5 °C on the onset day. 32 CAO events are obtained by this procedure. We rank these 32 events from

lowest to highest sum of NmTmn values (Table 1 in Appendix A). This sum only uses stations meeting the 5% NmTmn criterion.

Hartmann and Wendler (2005) investigated the significance of the 1976/1977 climate shift, which refers to that the Pacific Decadal Oscillation (PDO) index shifted from dominantly negative values for the 25-year time period (1951-75) to dominantly positive values for the period 1977-2001, for the climatology of Alaska. They found that the time means of several meteorology variables (i.e. temperature, wind, sea level pressure, geopotential height) are distinctly different between the two time periods above. As we use composite technique in the present study, we prefer to group the CAOs into two groups (before and after 1979) simply based on the onset date of the events to avoid the impact of the complexity of this climate shift on the dynamical analysis here. Thus, only the strong 10 CAO events after 1979 (Table 1) are studied here. Other events before 1979, which can be a comparison to this study, might be investigated later.

Event No.	Onset date
1	19901221
2	19890205
3	20070112
4	19981221
5	20120116
6	20110227
7	20020130
8	20091208

9	20130113
10	19870116

Table 1: Onset date of the strong 10 CAOs 1979-2013

2.2.2 Temperature tendency equation

With the aim of finding out the physical contributions to the temperature decrease in the CCV, we calculate each term of the temperature tendency equation. The procedure of how we do the calculation is given below. Step 1: NCEP-NCAR reanalysis 1 dataset is regridded to 1x1 degree resolution. Step 2: Horizontal temperature advection ($-u \frac{\partial \theta}{\partial x} - v \frac{\partial \theta}{\partial y}$) is calculated with method of spherical harmonics; Vertical temperature advection ($-\omega \frac{\partial \theta}{\partial p}$) is calculated with finite difference with a fourth order accuracy. Before calculating the vertical temperature advection, potential temperature and omega are interpolated with cubic spline method to obtain equally spaced data in pressure with interval 25hPa. Then both horizontal and vertical temperature advection are averaged over the 24-hour interval before adding them together to obtain the three dimensional temperature advection. Step 3: Local change term ($\frac{\partial \theta}{\partial t}$) of temperature equation is calculated with backward finite difference with a 24 hour interval. Step 4: Diabatic term ($Q = \frac{\partial \theta}{\partial t} + u \frac{\partial \theta}{\partial x} + v \frac{\partial \theta}{\partial y} + \omega \frac{\partial \theta}{\partial p}$) is approximated as a residual. Step 5: After temperature equation terms for each event are calculated, composite of the 10 events is made for each term.

The flux form of temperature equation was also tested by us. However, it is too noisy to see the general pattern (not shown here). This might be due to the numerical evaluation of derivatives of wind fields (i.e. $\frac{\partial u \theta}{\partial x}$) in the advection terms.

2.2.3 Small amplitude wave activity flux

While the temperature tendency equation shows us how the cold air moves and forms, the dynamic diagnostic method of wave activity flux (WAF) is being used to understand better how the LSMPs at upper level evolve. The phase-independent WAF developed by Takaya and Nakamura (2001) (hereafter TN2001) is aimed for stationary or migratory eddies on a zonally varying basic state, rather than zonally uniform basic state like other methods of WAF. Since neither zonal mean (i.e. Eliassen-Palm flux, Andrews and McIntyre 1976; Edmon et al 1980) nor time mean (i.e. the wave activity flux developed by Plumb 1986) is used in their development of the wave activity conservation equation, WAF of TN2001 is considered as a more suitable and realistic method for many research problems, such as storm tracking, blocking and so on. Compared with other linear methods of small amplitude WAF (Table 2), another advantage of Takaya and Nakamura's method is that it allows one to do snapshot analysis as the feature of phase independence doesn't involve any time averaging. With snapshot analysis, we can track the evolution of LSMPs associated with CAOs based on the parallel relationship of direction between wave group velocity and WAF. However, unlike E-P flux, the WAF of TN2001 can only tell the energy origin without any information of contributions of heat or momentum flux.

Small Amplitude Wave Activity Flux				
Methods	Dimension of Propagation	Basic Mean Flow	Snapshot Analysis	Phase Independence
E-P Flux (Andrews and McIntyre 1976; Edmon et al 1980)	Two dimensional	Zonally uniform	Yes	Yes

Extended E-P Flux (Hoskins et al 1983; Trenberth 1986)	Three dimensional	Zonally asymmetric	No	Yes (by time mean)
Plumb 1985	Three dimensional	Zonally uniform	No	Yes
Plumb 1986	Three dimensional	Zonally asymmetric	No	Yes (by time mean)
Takaya and Nakamura 2001	Three dimensional	Zonally asymmetric	Yes	Yes

Table 2: The table above is a simple summary of various dynamic analysis methods of WAF which are often used to analyze the interaction between mean flow and eddies. Among these different methods, WAF of TN2001 is used by us to analyze the role of eddies in forming the LSMPs associated with CAOs. We evaluate WAF of TN2001 at two levels (500hPa and 700hPa) over day -5 (5 days before the onset) to the onset.

Wave activity in TN2001 is defined in the way that it is proportional to the wave energy and the wave enstrophy which is related to squared quasi geostrophic potential vorticity anomaly. Via the linear relation ($\psi = \Phi/f$) between geostrophic stream function Φ and geopotential ψ and the relation between vertical stream function gradient and potential temperature ($\frac{\partial\psi}{\partial z} \propto \theta$), the wave activity carries information of both geopotential perturbation and temperature perturbation.

2.2.4 Finite amplitude wave activity

Different from linear methods of small amplitude wave activity flux, a few of finite amplitude wave activities have been defined in order to be able to describe the interactions between the basic flow and eddy perturbations of arbitrary amplitude. In particular, Nakamura

and Zhu (2010) developed a finite amplitude wave activity (FAWA) based on the meridional displacement of a potential vorticity (PV) contour from its “equivalent latitude” (Butchart and Remsburg 1986; Allen and Nakamura 2003) with the assumption that PV is increasing with latitude and that the contour of PV is parallel with the latitude circle in the absence of eddy perturbations. As it is an area integration of PV, their FAWA is not convenient for detecting and explaining the local phenomenon, i.e. blocking. Huang and Nakamura (2016) generalized the FAWA to local wave activity (LWA) by reducing the dimension of integration from area integration to line integration. Thus, LWA becomes Eulerian in longitude and is suitable for investigating regional weather events.

Since no linearization is used in the development of either FAWA or LWA, we view the result of LWA as a nonlinear counterpart of WAF described in the above section. As LWA is not based on linearized PV equation, it does not hold any indicative relation between wave activity flux and group velocity which is the point of how WAF has often been used in current literatures. In other words, in derivation of WAF of TN2001 there are two following crucial elements: (i) linearization of QGPV equation (FAWA starts from the fully nonlinear PV equation and could work outside of quasi-geostrophic framework); (ii) plane wave representation of perturbation field under the WKB limit of weakly dissipated, slowly varying waves (the mathematical representation of waves for FAWA is not limited). These two conditions of WAF are basic steps for the dispersion relation needed for the derivation of group velocity and thus for the parallel relation between the directions of group velocity and WAF. However, they are not applicable to the development of FAWA.

We evaluated quasi-geostrophic potential vorticity (Andrews et al 1987, their equation (3.2.15); Huang and Nakamura 2016, their equation (3)) on 33 equally spaced pressure

pseudoheights as described in Nakamura and Solomon (2010). The difference is that our pressure domain is from 1000hPa to 10hPa rather than 1000hPa to 1hPa. Then equivalent latitude is calculated (Butchart and Remsberg 1986; Allen and Nakamura 2003, their equation (1); Nakamura and Zhu 2010, their equation (10)). LWA is evaluated as equation (13) in Huang and Nakamura (2016). The LWA at 320hPa over day -5 (5 days before the onset) to the onset is shown in this study.

3. Results

3.1 Temperature tendency equation

As shown in figure 3.1.1, cold advection dominates the California Central Valley (CCV) starting from 4 days prior to the onset. The center of the cold advection first moves southeastward over day -4 to day -2 and then moves westward to arrive in the CCV on day -1. The movement of this core of cold advection is consistent with that of flow of unusual cold

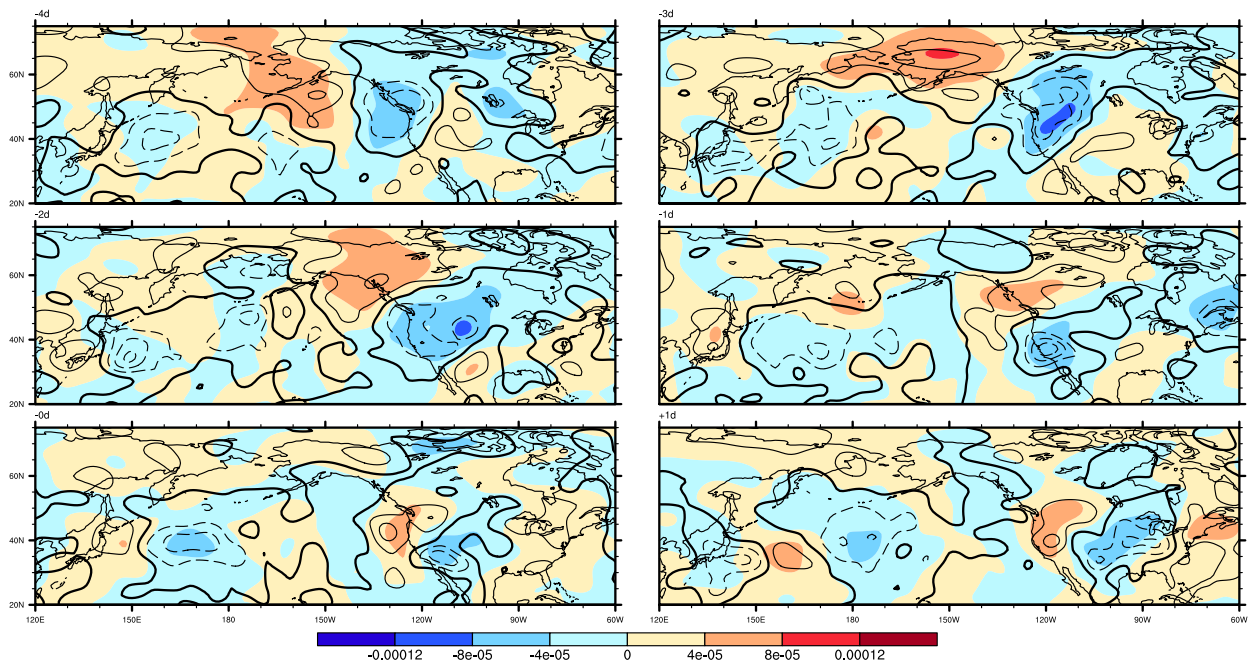


Fig 3.1.1 Composites of the 10 CAOs for local change term (shading) and three dimensional temperature advection (contour) at 700hPa. Negative values have dashed contours while positive values use solid contours. Contour and shading intervals are both 0.00004 K/s. The string ‘-Nd’ (‘+Nd’) in the upper left corner of each map denotes N days prior to (after) the onset (all times are 12 UTC).

found in part I, which moves southeastward and then westward to the Pacific Northwest and California to create the CAOs. In contrast, warm advection happens over the CCV right after the onset (day +1). There is a strong warm advection over the Bering sea and western Alaska on day -4, which expands eastward and intensifies quickly in the Gulf of Alaska on day -3. This warm advection favors the formation of the ridge over the Alaskan region in middle and upper troposphere (i.e. figure 3.2.3 in Part I).

The general pattern of temperature advection at 850hPa (figure 1 in Appendix B) is quite similar to that of 700hPa. However, thermal advection over the Alaskan region at 850hPa is stronger than that of 700hPa at day -4 and day -3. Diabatic heating, which is calculated as a

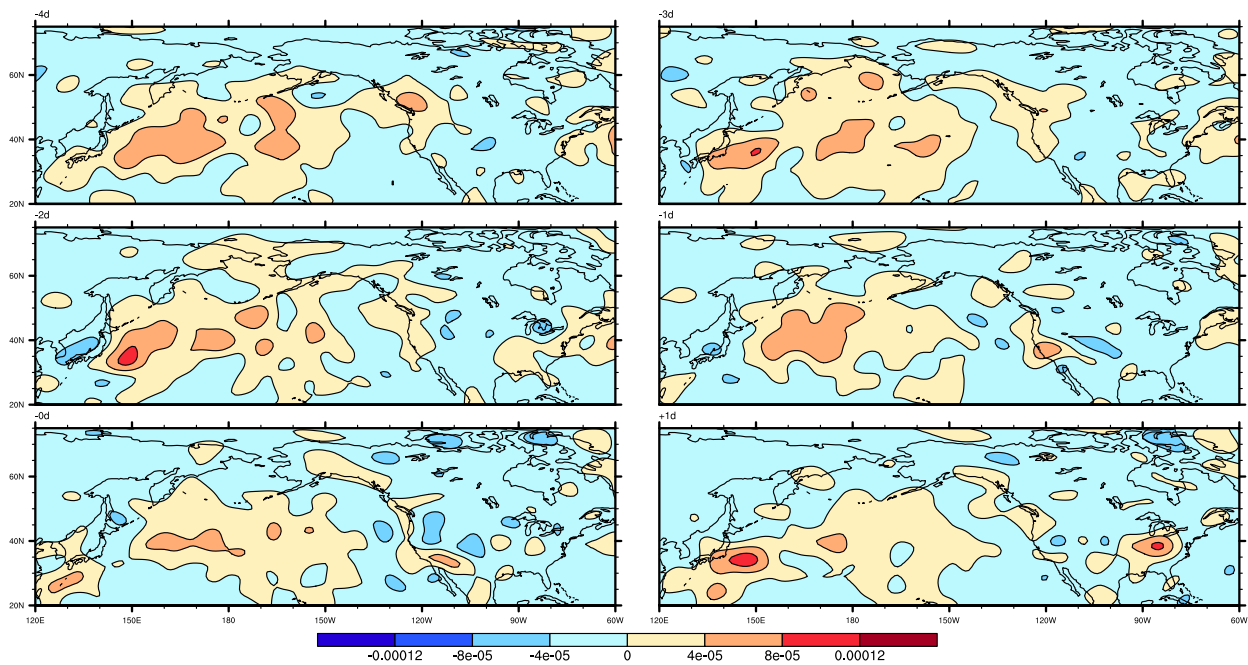


Fig 3.1.2 Composites of the 10 CAOs for diabatic term at 700hPa. Contour interval is 0.00004 K/s. The string ‘-Nd’ (‘+Nd’) in the upper left corner of each map denotes N days prior to (after) the onset (all times are 12 UTC).

residual, is much smaller than temperature advection at both the upper and lower levels (figure 3.1.2 and figure 2 in Appendix B). Thus, although diabatic warming is seen over CCV at both levels, it barely counteracts the cooling by advection. Therefore, cold temperature advection is the dominant process in the formation of CAOs in the CCV. Consistently, Colle and Mass (1995) also found that cold advection is dominant although their calculation was based on model output and they investigated CAOs east of the Rocky Mountains.

3.2 Small amplitude wave activity flux

In part I, we have shown that the areas of cold anomaly and warm anomaly are equivalent barotropic and therefore have associated upper level trough and ridge anomalies, respectively. To learn more about how the LSMPs of geopotential height anomaly evolve at a higher level, we present the result of WAF of TN2001 in this subsection.

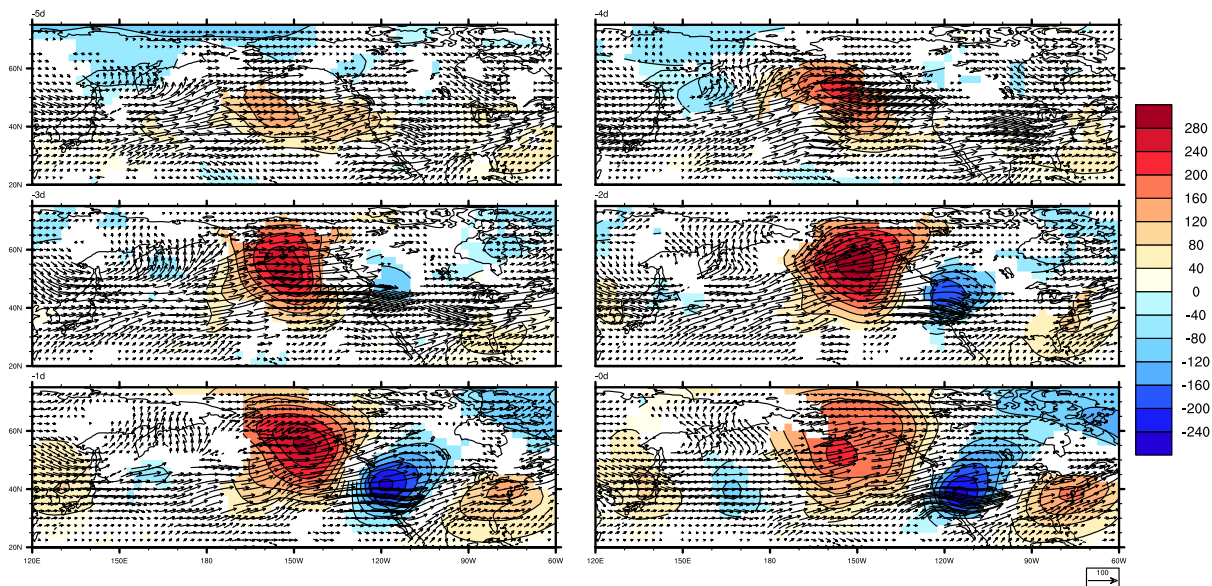


Fig 3.2.1 Composites of the 10 CAOs for geopotential height anomaly (m; contours with color shading) and stationary part of horizontal WAF (m^2s^{-2} ; vectors) at 500hPa from 5 days before the onset (upper left) to the onset (lower right). All times are 12 UTC. Geopotential height anomaly is plotted at grid points where at least 2/3 of the events have the same sign. WAF is plotted when at least one of zonal or meridional component has same sign for at least 2/3 of the events. Contour interval is 40m.

Since the wave activity flux (WAF) parallels the group velocity, the vectors illustrate the propagation of the wave trains. Convergence (divergence) of WAF indicates piling up (exporting) of wave activity. In figure 3.2.1, convergence of WAF over the North Pacific amplifies Gulf of Alaska ridge more on its north side of ridge while propagating northeastward over day -5 to day -4. Meanwhile, the shape of this ridge becomes more elliptic as its southeastern tail is diminished by the divergence of WAF off the western coast. Over day -4 to day -3, the axis of the ridge is rotated to the right to parallel the meridional line by the WAF with orientation SW-NE on its west side and WAF oriented NW-SE on its northeast side. The ridge is elongated along the longitude as the WAF oriented NW-SE becomes eastward on day -3. Over day -3 to day -2, the ridge continues to strengthen and expand in latitude by the quickly enlarged WAF over the Gulf of Alaska and western Canada. At the same time, the trough over the western coast is built by the WAF convergence near the western coast while moving southeastward. Over day -2 to day -1, the strengthened trough has a NE-SW axis on its northern part due to the quickly enlarged WAF on its northwest side. The southern part of this trough is expanded and strengthened by the unusually large eastward WAF. East of this trough, the intensified WAF with its direction changing from eastward to northeastward over northwestern Mexico and south-central US builds the ridge over the southeast of the US. Over day -1 to the onset, the southeastern ridge continues to strengthen in the same way. The ridge over the Alaskan region expands to its largest size with the core decreasing, which is consistent with the lessened WAF

west of the ridge. In short, the patterns of WAF help us to explain the evolution of LSMPs of geopotential height anomaly at 500hPa. Also, there is a noticeable hint at the energy source from the subtropics, especially at day -3 and day -2.

The patterns of geopotential height anomaly and WAF at 700hPa (figure 3 in Appendix B) are quite similar to that of 500hPa. The main difference is that the intensities of geopotential height anomaly and WAF are both weaker at 700hPa than 500hPa. Equivalent barotropic feature can be seen as there are no axis tilt for the Gulf of Alaska ridge. Similarly, Lau and Lau (1984) also found that the low frequency fluctuations accompanying the cold air breaks have equivalent barotropic feature.

3.3 Quasi-geostrophic potential vorticity

Temperature tendency equation and WAF have shown how the cold air forms and moves at lower levels and how the mass fields evolve in the mid troposphere, respectively. In this subsection, we use QGPV as a descriptive variable, rather than a diagnostic variable as in the potential vorticity equations, to examine the evolution patterns of QGPV for individual event at 320hPa with the hope of gaining more knowledge of development of CAOs at upper levels.

All events have the trough-ridge-trough pattern of QGPV over the Alaskan region-western coast-southeastern US either at onset or on day -1 (figure 3.3.1 and figure 3.3.2) corresponding to the LSMPs of geopotential height anomaly, though event 5 (at onset) and event 6 (day -1) have the core of the QGPV trough far west to Alaska. As shown in figure 3.3.1 and figure 3.3.2, different events tend to have different evolution patterns of QGPV before the onset. However, it is interesting to find common features shared by certain events. Three events (event number 4, 8 and 10) have a QGPV trough south of Alaska at day -5, which moves northward to

cover the whole Alaska in the following days and strengthens along the way sometimes. Four events (event number 1, 3, 5 and 9) have a source of QGPV trough just southwest or far southwest of Alaska at day -5, and then this QGPV trough moves northeastward to cover part of

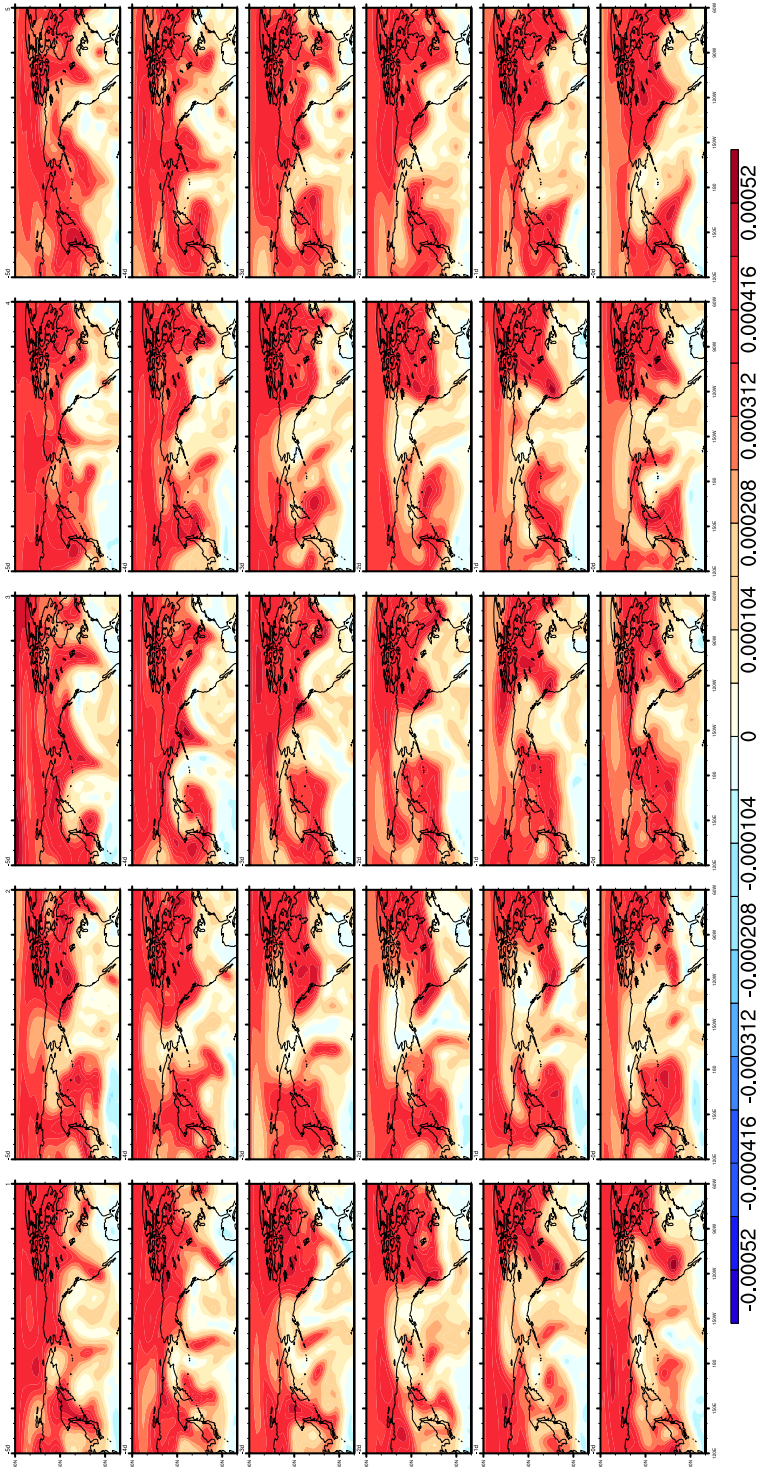


Fig 3.3.1 This figure is rotated 90° to the left to fit onto the page. Quasi geostrophic potential vorticity for individual CAOs at 320hPa. The number in the upper right corner of each column indicates the event number listed in Table 1. The string ‘-Nd’ in the upper left corner of each map denotes N days prior to the onset (all times are 12 UTC). The shading interval is $5.2 \times 10^{-5} s^{-1}$.

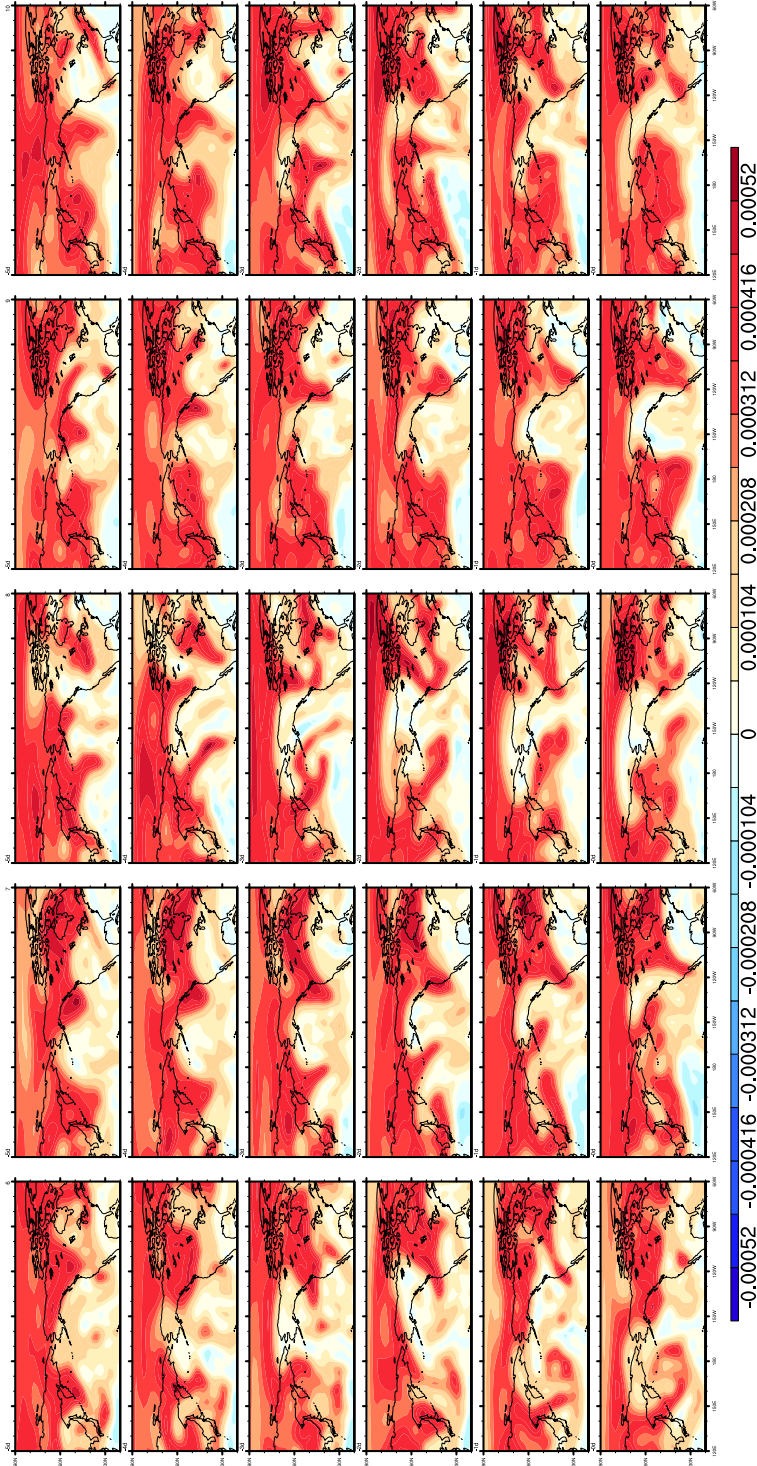


Fig 3.3.2 Same as figure 3.3.1 but for event 6 to 10 (Table 1).

or all of the Alaskan region. Sometimes this QGPV trough emerges with the QGPV low in Gulf of Alaska or expands to the region far west of Alaska. In this group, we see some tropical connections as shown in section 3.2 and will be shown in section 3.5. For example, in event 5, the origin of the QGPV trough lies in the subtropical region at day -5 and then quickly ejects northward. The other three events (event number 2, 6 and 7) seem to have the QGPV trough right in place several days before with little movement compared with other groups. The southward intrusions of the high QGPV from the Polar region into the CCV also vary a little bit among events. However, most of them intrude into the CCV while sharpening the shape of the QGPV ridge towards the onset.

3.4 Finite amplitude local wave activity

Sillmann et al. (2011) improved the fit of generalized extreme value distribution to negated extreme winter minimum temperature (2m) in large parts of European by including atmospheric blocking over North Atlantic as a covariate. The LSMPs associated with CAOs, as stated in Grotjahn et al (2015), often has some portion similar to a blocking ridge. Thus a blocking index can be a LSMP indicator. The evolution of the ridge over the Alaskan region, which is described in part I and similar to a blocking ridge, is crucial for the occurrence of CAOs by disturbing a predominant westerly flow and allowing a northerly inflow of cold air. In this subsection, we use the finite amplitude local wave activity developed in Huang and Nakamura (2016) to identify the LSMPs.

The northward intrusion of a trough of the QGPV towards the Alaskan region is accompanied by the formation of a QGPV ridge over the west coast (figure 3.4.1). The QGPV trough in the southeastern America seems to be in place a few days before. Towards onset, the

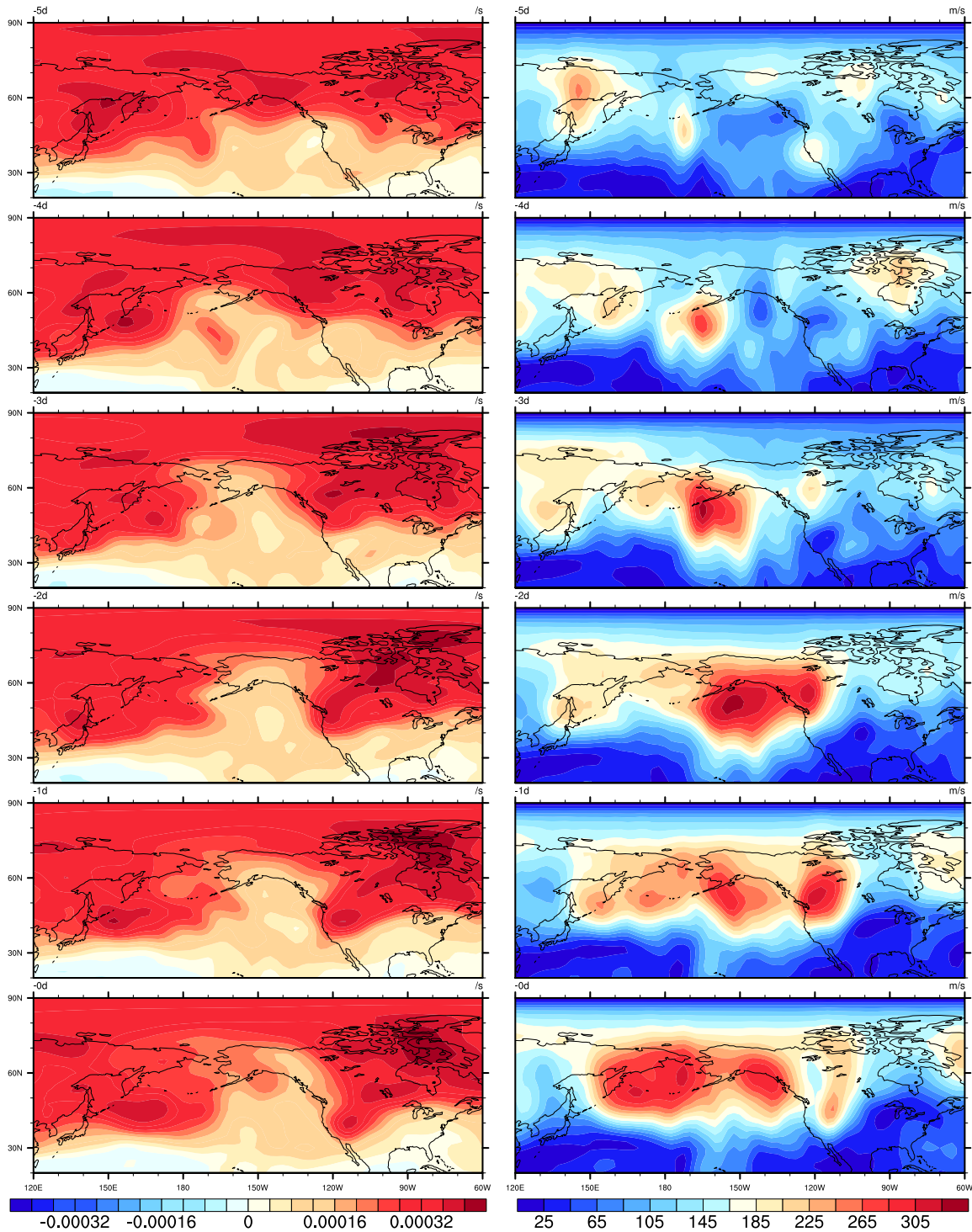


Fig 3.4.1 Composites of the 10 CAOs for quasi geostrophic potential vorticity (left) and local wave activity (right) at 320hPa. The shading intervals are respectively $4.0 \times 10^{-5} s^{-1}$ and 20 m/s. The string '-Nd' in the upper left corner of each map denotes N days prior to the onset (all times are 12 UTC).

west part of the QGPV trough over the Alaskan region seems to dilute to cover more area to the west of Alaska and Bering sea. The general pattern of the QGPV field explains the LSMPs of geopotential height anomaly found in part I. Consistent with the evolution of the pattern of QGPV, the LWA over North Pacific strengthens gradually and meanwhile expands in both longitude and latitude over day -5 to day -3 (figure 3.4.1). Over day -2 to the onset, another local maximum of LWA, which seems to split from the maximum of LWA over Alaskan region, develops over the western coast corresponding to the QGPV ridge in that region and moves into the CCV near onset. At onset, there is a noticeable expansion of the maximum of LWA over the Bering sea corresponding to the expansion of QGPV trough over the same region. In short, LWA shown in figure 3.4.1 captures well the reversion of the QGPV gradient which is highly related to the LSMPs of geopotential height anomalies. The QGPV and LWA fields (figure 3.4.1) matches well with each other in the same sense as in Huang and Nakamura (2016).

3.5 Divergent wind components

Strong extratropical response to the tropical divergence source in the upper troposphere are found in both linear and fully nonlinear model (Sardeshmukh and Hoskins 1988). Also, they showed that Rossby wave source can be remote from the heating region due to the movement of the corresponding divergence source into the subtropics. Inspired by their work, we attempt to find if there is a tropical or subtropical divergence source related to the LSMPs.

Notable northwesterlies are seen to move southeastward over the western US over day -5 to -2, with convergence ahead causing sinking and divergence behind with rising (figure 3.5.1). Over day -3 to the onset, there are noticeable divergent winds coming from the tropical region over eastern subtropical Pacific, which are especially evident on day -1. The easterly divergent

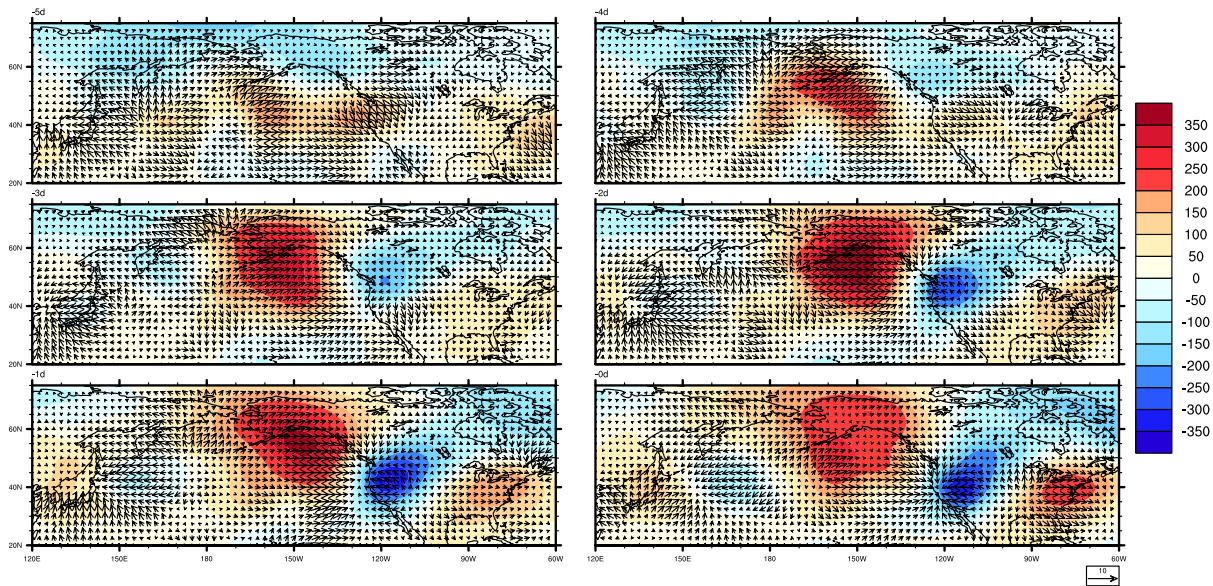


Fig 3.5.1 Composites of the 10 CAOs for geopotential height anomaly (m; color shadings) and divergent wind components (m/s; vectors) at 300hPa. The string ‘-Nd’ in the upper left corner of each map denotes N days prior to the onset (all times are 12 UTC).

winds over northwestern US on day -2 and day -1 are consistent with the sinking on the west side of the trough more than the other sides. There is also a notable divergence source in the central North Pacific at the southwest corner of the Alaskan ridge. This upper level divergence source is consistent with the rising motions seen in the same region in Part I.

4. Discussion and Conclusion

The temperature tendency equation shows that cold advection is the dominant process leading to the CAOs in the CCV, which is consistent with the result of Colle and Mass (1995)

though their result is based on model output and focuses on the CAOs east of the Rocky Mountains). Strong warm advection over the Bering sea and western Alaska on day -4, which expands eastward and intensifies quickly in the Gulf of Alaska on day -3, favors the formation of the ridge over the Alaskan region.

The patterns of wave activity flux explain the evolution of LSMPs of geopotential height anomalies. Convergence of WAF over the North Pacific amplifies Gulf of Alaska ridge more on its north side of ridge while propagating northeastward over day -5 to day -4. The ridge continues to strengthen and expand in latitude by the quickly enlarged WAF over the Gulf of Alaska and western Canada over day -3 to day -2. Meanwhile, the trough over the western coast is built by the WAF convergence near the western coast while moving southeastward. East of this trough, the intensified WAF with its direction changing from eastward to northeastward over northwestern Mexico and south-central US builds the ridge over the southeast of the US over day -2 to day -1. In addition, there is a noticeable hint at the energy source from the subtropics, especially on day -3 and day -2.

Whereas inspection of the QGPV figures for individual events does indicate some degree of variability from case to case, the trough-ridge-trough patterns of QGPV over the Alaskan region-western coast-southeastern US at onset corresponding to the ridge-trough-ridge patterns of geopotential height anomalies are also discernible in almost all the events. The evolutions of the trough of QGPV over the Alaskan region for certain events appear to show a subtropical connection. The southward intrusion of high QGPV from the Polar region into the CCV to form a local maximum of QGPV are found in most events although the way they do it varies a little bit.

The LWA over North Pacific strengthens gradually and meanwhile expands in area over day -5 to day -3. Another local maximum of LWA, which seems to split from the maximum of LWA over Alaskan region, develops over the western coast corresponding to the QGPV ridge in that region and moves into the CCV near onset. The LWA captures well the reversion of the QGPV gradient which is highly related to the LSMPs of geopotential height anomalies. Also, the QGPV and LWA fields matches well with each other in the same sense as in Huang and Nakamura (2016).

Notable northwesterlies are seen to move southeastward over the western US over day -5 to -2. There are noticeable divergent winds coming from the tropical region over eastern subtropical Pacific over day -3 to the onset, which are especially evident on day -1. As noted above, this kind of subtropical source hint is also seen in the evolution of QGPV for some individual events and the evolution patterns of composite WAF.

References

Andrews D. G., J. R. Holton, and C. B. Leovy, 1987: Middle Atmosphere Dynamics. Academic Press, 489 pp.

Andrews, D. G., and M. E. McIntyre, 1976: Planetary waves in horizontal and vertical shear: The generalized Eliassen–Palm relation and the mean zonal acceleration. *J. Atmos. Sci.*, 33, 2031–2048, doi: [10.1175/1520-0469\(1976\)033<2031:PWIHAV>2.0.CO;2](https://doi.org/10.1175/1520-0469(1976)033<2031:PWIHAV>2.0.CO;2).

Allen D. R., and N. Nakamura, 2003: Tracer equivalent latitude: A diagnostic tool for isentropic transport studies. *J. Atmos. Sci.*, 60, 287–304, doi:[10.1175/1520-0469\(2003\)060,0287:TELADT.2.0.CO;2](https://doi.org/10.1175/1520-0469(2003)060,0287:TELADT.2.0.CO;2).

Bueh C., N. Shi, and Z. Xie, 2011: Large-scale circulation anomalies associated with persistent low temperature over Southern China in January 2008. *Atmos. Sci. Lett.*, 12, 273–280, doi:[10.1002/asl.333](https://doi.org/10.1002/asl.333).

Butchart N., and E. Remsberg, 1986: The area of the stratospheric polar vortex as a diagnostic for tracer transport on an isentropic surface. *J. Atmos. Sci.*, 43, 1319–1339, doi:[10.1175/1520-0469\(1986\)043,1319:TAOTSP.2.0.CO;2](https://doi.org/10.1175/1520-0469(1986)043,1319:TAOTSP.2.0.CO;2).

Colle B. A., and C. F. Mass, 1995: The structure and evolution of cold surges east of the Rocky Mountains. *Mon. Wea. Rev.*, 123, 2577–2610, doi:[10.1175/1520-0493\(1995\)123,2577:TSAEOC.2.0.CO;2](https://doi.org/10.1175/1520-0493(1995)123,2577:TSAEOC.2.0.CO;2).

Edmon H. J., B. J. Hoskins, and M. E. McIntyre, 1980: Eliassen–Palm cross sections for the troposphere. *J. Atmos. Sci.*, 37, 2600–2616; Corrigendum, 38, 1115, doi:[10.1175/1520-0469\(1980\)037<2600:EPCSFT>2.0.CO;2](https://doi.org/10.1175/1520-0469(1980)037<2600:EPCSFT>2.0.CO;2)

Grotjahn R., and G. Faure, 2008: Composite predictor maps of extraordinary weather events in the Sacramento, California, region. *Wea. Forecasting*, 23, 313–335, doi:[10.1175/2007WAF2006055.1](https://doi.org/10.1175/2007WAF2006055.1).

Hartmann B., and G. Wendler, 2005: The significance of the 1976 Pacific climate shift in the climatology of Alaska, *J. Clim.*, 18, 4824–4839, doi:[10.1175/JCLI3532.1](https://doi.org/10.1175/JCLI3532.1).

Hoskins, B. J., I. N. James, and G. H. White, 1983: The shape, propagation and mean-flow interaction of large-scale weather systems. *J. Atmos. Sci.*, 40, 1595–1612, doi:[10.1175/1520-0469\(1983\)040<1595:TSPAMF>2.0.CO;2](https://doi.org/10.1175/1520-0469(1983)040<1595:TSPAMF>2.0.CO;2).

Huang C. S. Y., and N. Nakamura, 2016: Local finite-amplitude wave activity as a diagnostic of anomalous weather events, *J. Atmos. Sci.*, doi:[10.1175/JAS-D-15-0194.1](https://doi.org/10.1175/JAS-D-15-0194.1).

Kalnay E., and Coauthors, 1996: The NCEP/NCAR 40-Year Reanalysis Project. *Bull. Amer. Meteor. Soc.*, 77, 437–471, doi:[10.1175/1520-0477\(1996\)077,0437:TNYRP.2.0.CO;2](https://doi.org/10.1175/1520-0477(1996)077,0437:TNYRP.2.0.CO;2).

Lau N.-C., and K.-M. Lau, 1984: The structure and energetics of midlatitude disturbance accompanying cold-air outbreaks over East Asia. *Mon. Wea. Rev.*, 112, 1309–1327, doi:[10.1175/1520-0493\(1984\)112<1309:TSAEOM>2.0.CO;2](https://doi.org/10.1175/1520-0493(1984)112<1309:TSAEOM>2.0.CO;2)

Nakamura N., and A. Solomon, 2010: Finite-amplitude wave activity and mean flow adjustments in the atmospheric general circulation. Part I: Quasigeostrophic theory and analysis. *J. Atmos. Sci.*, 67, 3967–3983, doi:[10.1175/2010JAS3503.1](https://doi.org/10.1175/2010JAS3503.1).

———, and D. Zhu, 2010: Finite-amplitude wave activity and diffusive flux of potential vorticity in eddy–mean flow interaction. *J. Atmos. Sci.*, 67, 2701–2716, doi:[10.1175/2010JAS3432.1](https://doi.org/10.1175/2010JAS3432.1).

Plumb R. A., 1985: On the three-dimensional propagation of stationary waves. *J. Atmos. Sci.*, 42, 217–229, doi:[10.1175/1520-0469\(1985\)042,0217:OTTDPO.2.0.CO;2](https://doi.org/10.1175/1520-0469(1985)042,0217:OTTDPO.2.0.CO;2).

Plumb R. A., 1986: Three-dimensional propagation of transient quasi-geostrophic eddies and its relationship with the eddy forcing of the time–mean flow. *J. Atmos. Sci.*, 43, 1657–1678, doi:[10.1175/1520-0469\(1986\)043,1657:TDPOTQ.2.0.CO;2](https://doi.org/10.1175/1520-0469(1986)043,1657:TDPOTQ.2.0.CO;2).

Sardeshmukh PD, Hoskins BJ, 1988: The generation of global rotational flow by steady idealized tropical divergence. *J Atmos Sci* 45:1228–1251, doi:[10.1175/1520-0469\(1988\)045<1228:TGOGRF>2.0.CO;2](https://doi.org/10.1175/1520-0469(1988)045<1228:TGOGRF>2.0.CO;2).

Sillmann J, Croci-Maspoli M, Kallache M, Katz RW, 2011: Extreme cold winter temperatures in Europe under the influence of North Atlantic atmospheric blocking. *J Clim* 24:5899–5913. doi:[10.1175/2011JCLI4075.1](https://doi.org/10.1175/2011JCLI4075.1)

Takaya K., and H. Nakamura, 2001: A formulation of a phase- independent wave-activity flux for stationary and migratory quasigeostrophic eddies on a zonally varying basic flow. *J. Atmos. Sci.*, 58, 608–627, doi:[10.1175/1520-0469\(2001\)058,0608:AFOAPI.2.0.CO;2](https://doi.org/10.1175/1520-0469(2001)058,0608:AFOAPI.2.0.CO;2).

Trenberth, K. E., 1986: An assessment of the impact of transient eddies on the zonal flow during a blocking episode using localized Eliassen–Palm flux diagnostics. *J. Atmos. Sci.*, 43, 2070–2087, doi: [10.1175/1520-0469\(1986\)043<2070:AAOTIO>2.0.CO;2](https://doi.org/10.1175/1520-0469(1986)043<2070:AAOTIO>2.0.CO;2).

Westby R. M., and R. X. Black, 2015: Development of Anomalous Temperature Regimes over the Southeastern United States: Synoptic Behavior and Role of Low-Frequency Modes. *Wea. Forecasting*, 30, 553-570, doi:[10.1175/WAF-D-14-00093.1](https://doi.org/10.1175/WAF-D-14-00093.1).

Acknowledgments

Firstly, I would like to give many sincere thanks to my advisor Prof. Richard Grotjahn for his guidance, encouragement and support during the development of this work. Without his mentoring and his immense knowledge in this area, it is impossible to have this present work done. Secondly, I am very grateful that Prof. Shuhua Chen and Prof. Paul Ullrich are willing to spare their precious time to be on my thesis committee and help improve this work by giving us great suggestions and comments. Also, I want to thank Dr. Yun-Young Lee for her discussions with me. This research was funded in part by NSF grant 1236681 and also supported by the USDA National Institute of Food and Agriculture, Hatch project CA-D-LAW-4264-H.

Appendix A

Ranking	Onset date						
1	19901221	9	20120116	17	19530220	25	19550219
2	19890205	10	19561208	18	20110227	26	20130113
3	20070112	11	19760101	19	19560216	27	19681221
4	19981221	12	19781207	20	20020130	28	19520102
5	19630112	13	19620122	21	19621226	29	19870116
6	19620226	14	19570130	22	19710226	30	19750102
7	19721208	15	19730105	23	20091208	31	19570109
8	19600101	16	19700105	24	19680104	32	19511209

Table 1 Onset date of 32 CAOs in 1951-2013. The number to the left of the onset date indicates the ranking of the event.

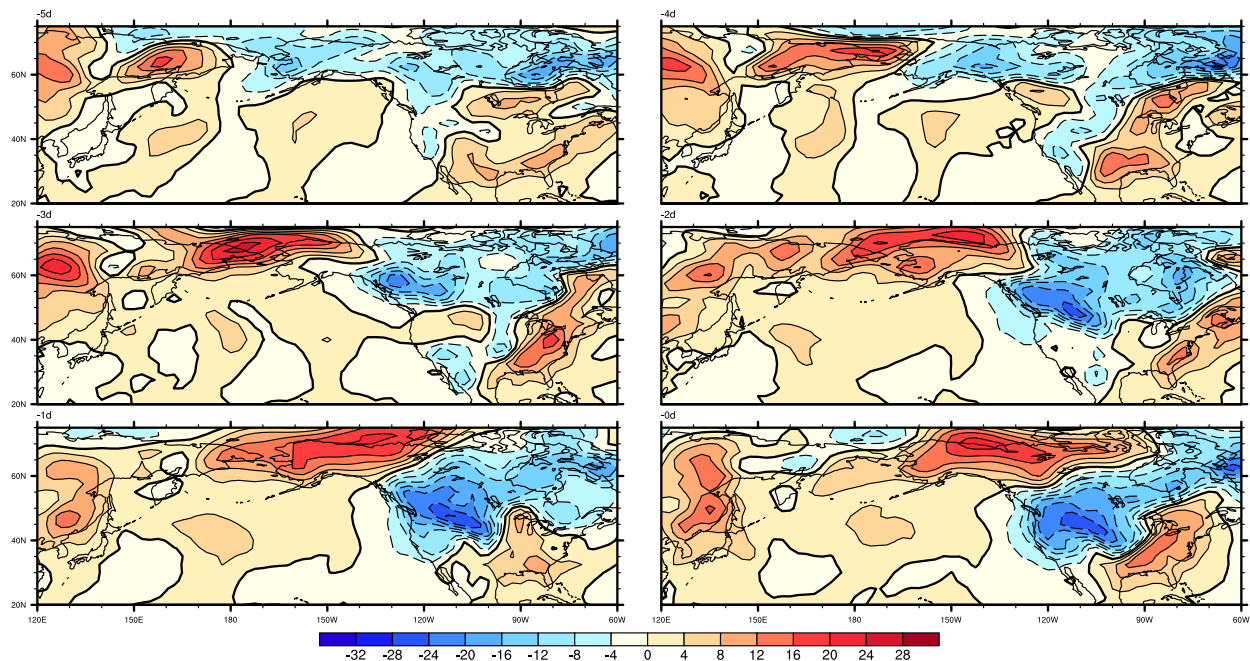


Fig 1 Surface temperature anomaly at sigma 0.995 for event 1 (Table 1) for days before the onset. The string '-Nd' in the upper left corner of each map denotes N days prior to the onset (all times are 12 UTC). The contour interval is 4K.

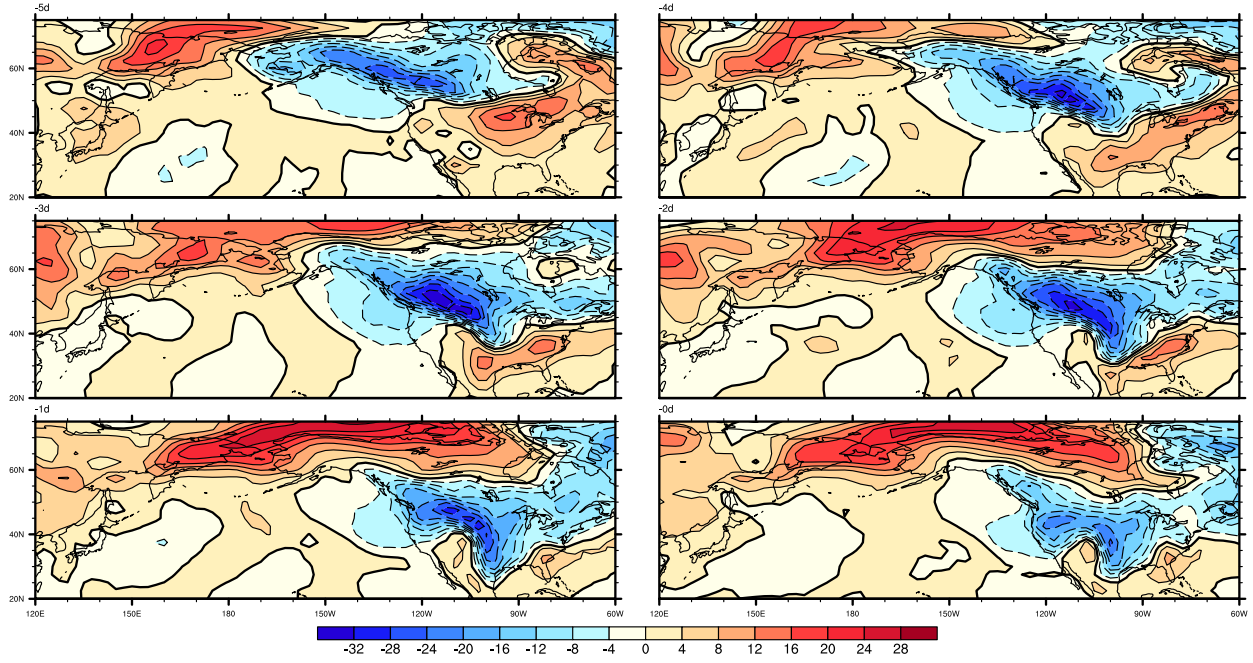


Fig 2 Same as Fig 1, but for event 2 (Table 1).

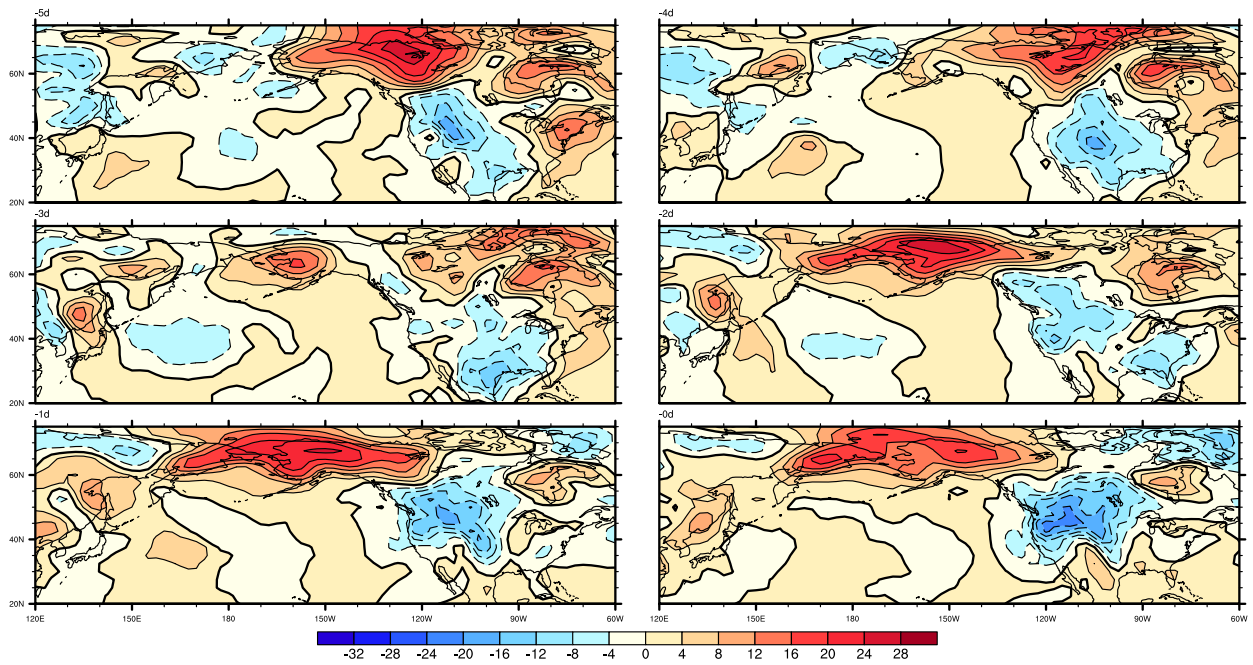


Fig 3 Same as Fig 1, but for event 8 (Table 1).

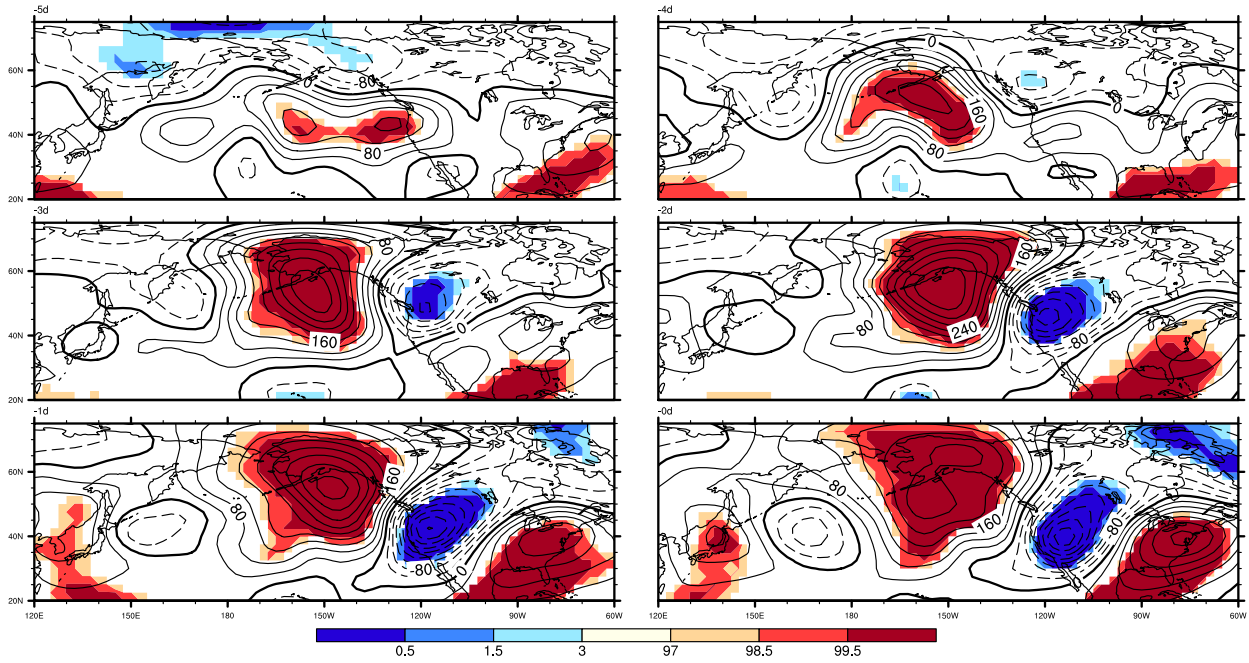


Fig 4 Same as figure 3.2.1, but for geopotential height anomaly at 300hPa.

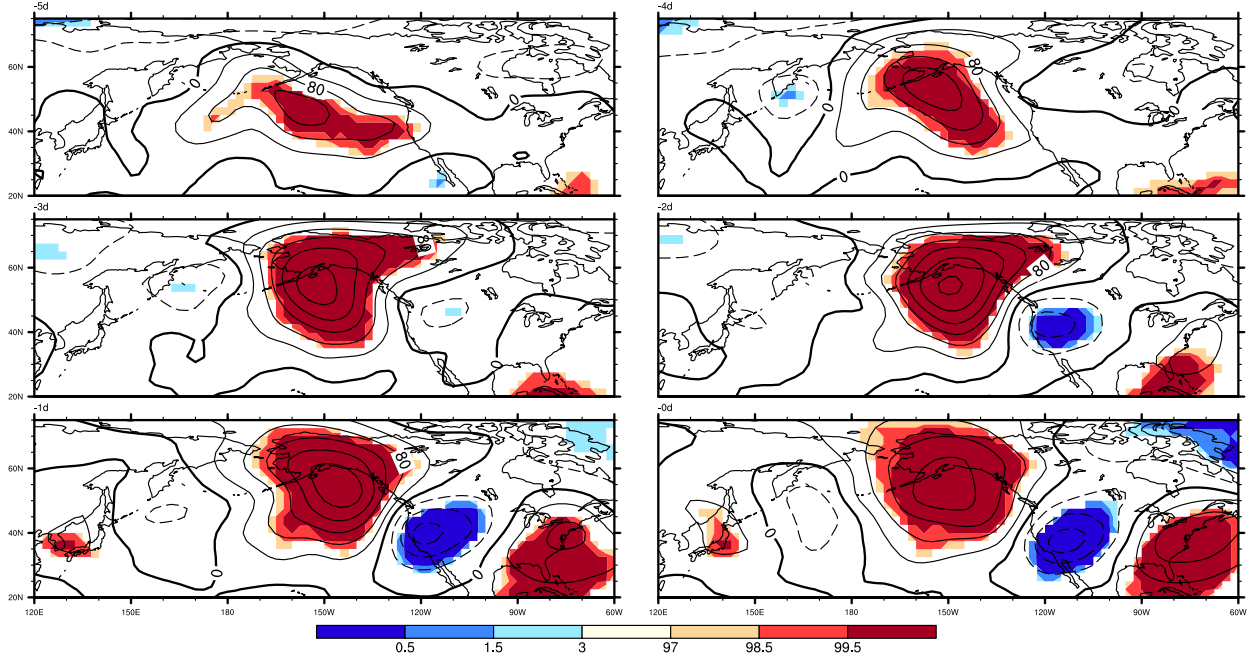


Fig 5 Same as figure 3.2.1, but for geopotential height anomaly at 700hPa.

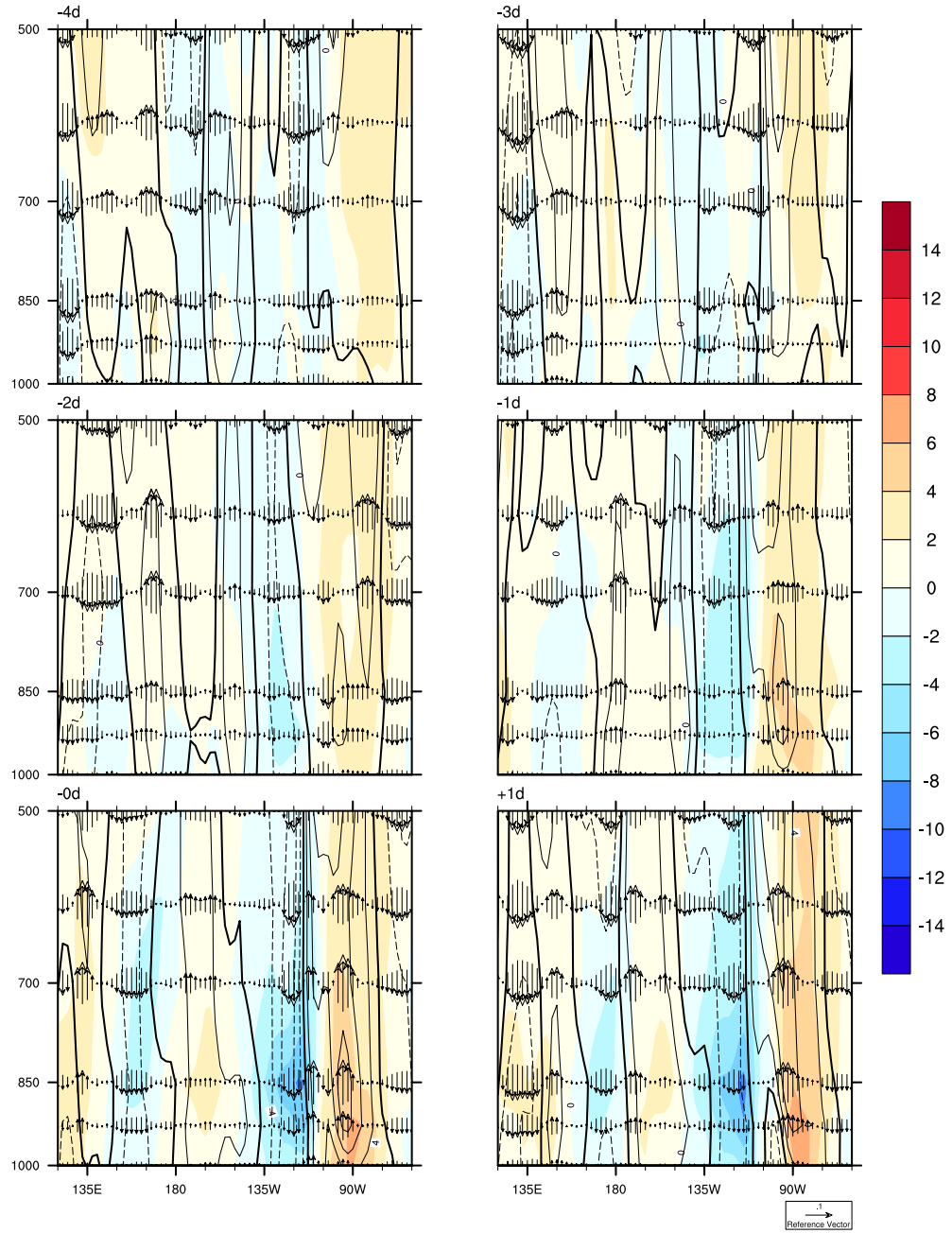


Fig 6 Same as figure 3.3.1, but at 30N.

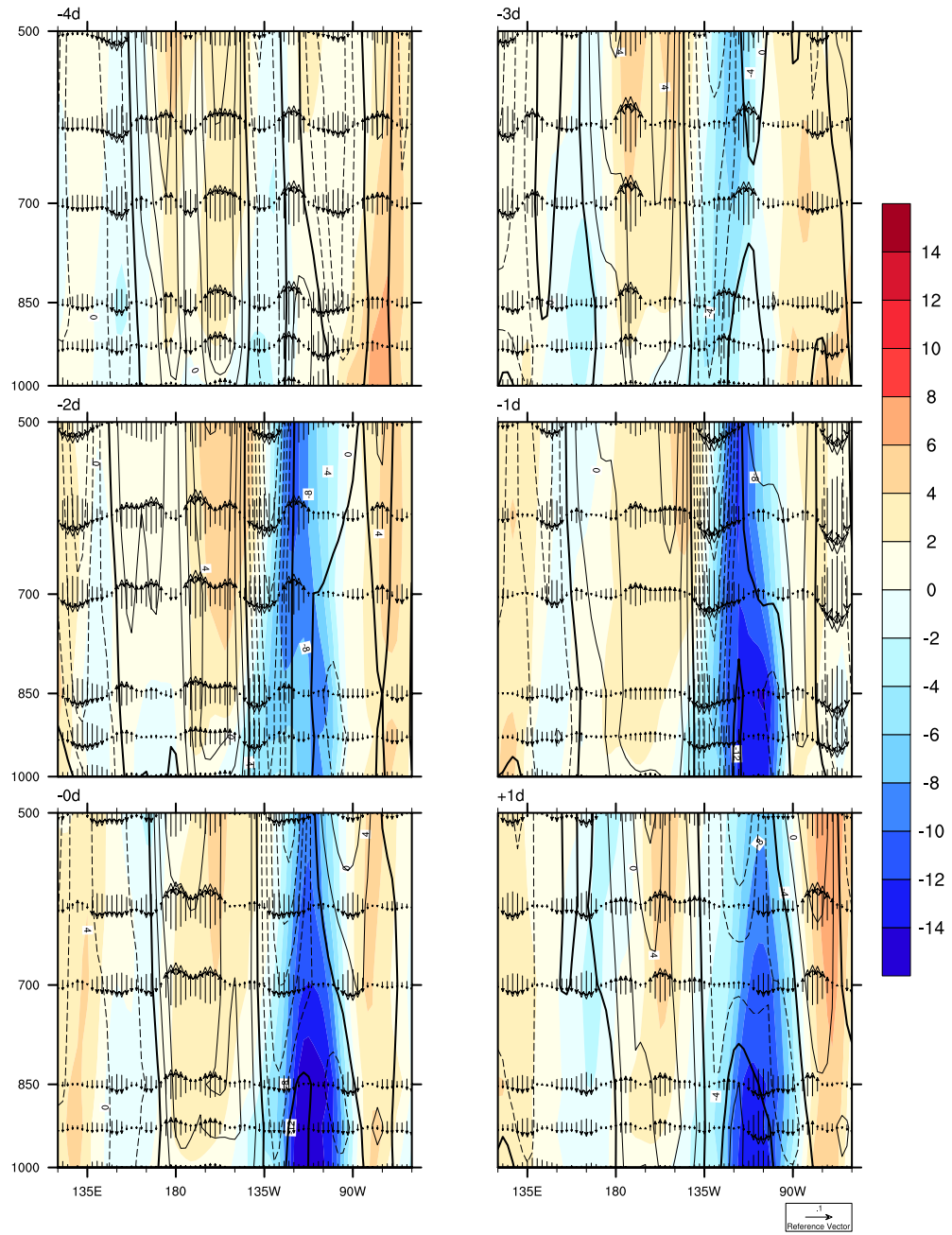


Fig 7 Same as figure 3.3.1, but at 45N.

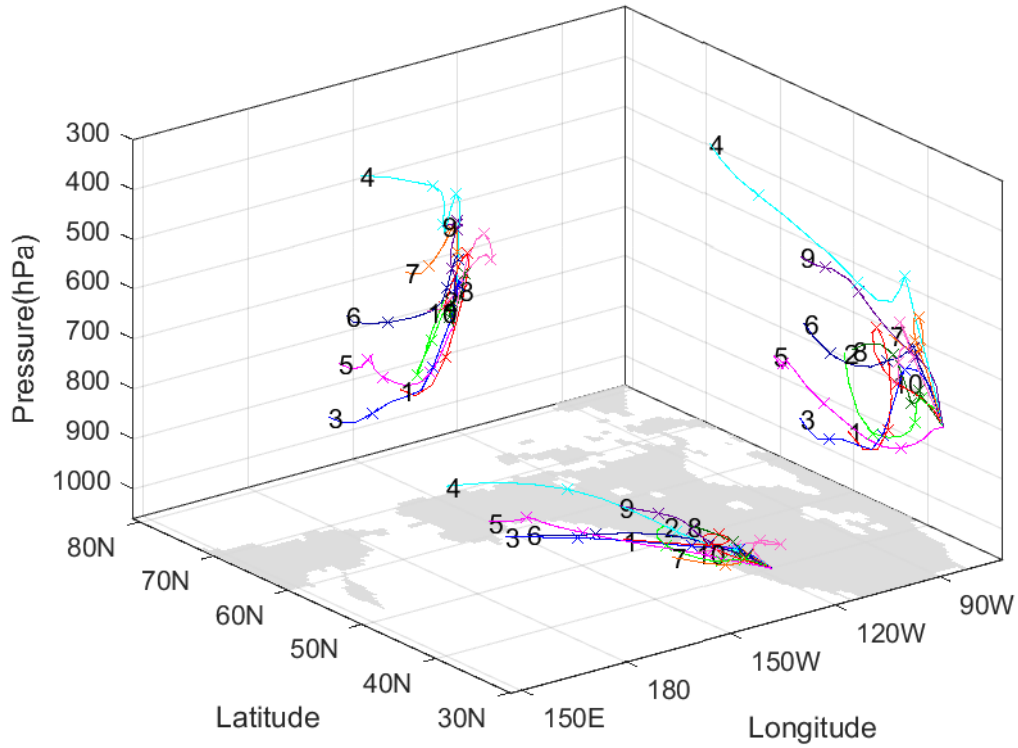


Fig 8 Same as figure 3.4.1, but for 850hPa.

Appendix B

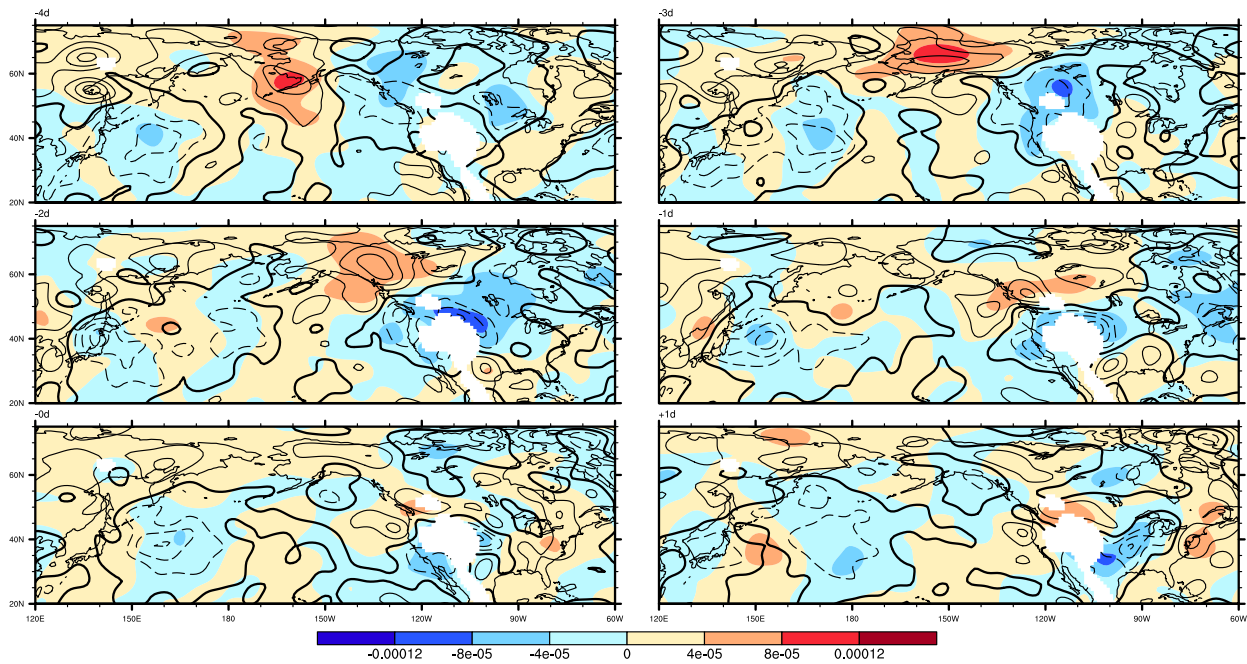


Fig 1 Same as figure 3.1.1, but for 850hPa. Regions with surface pressure lower than 850hPa are masked by white color.

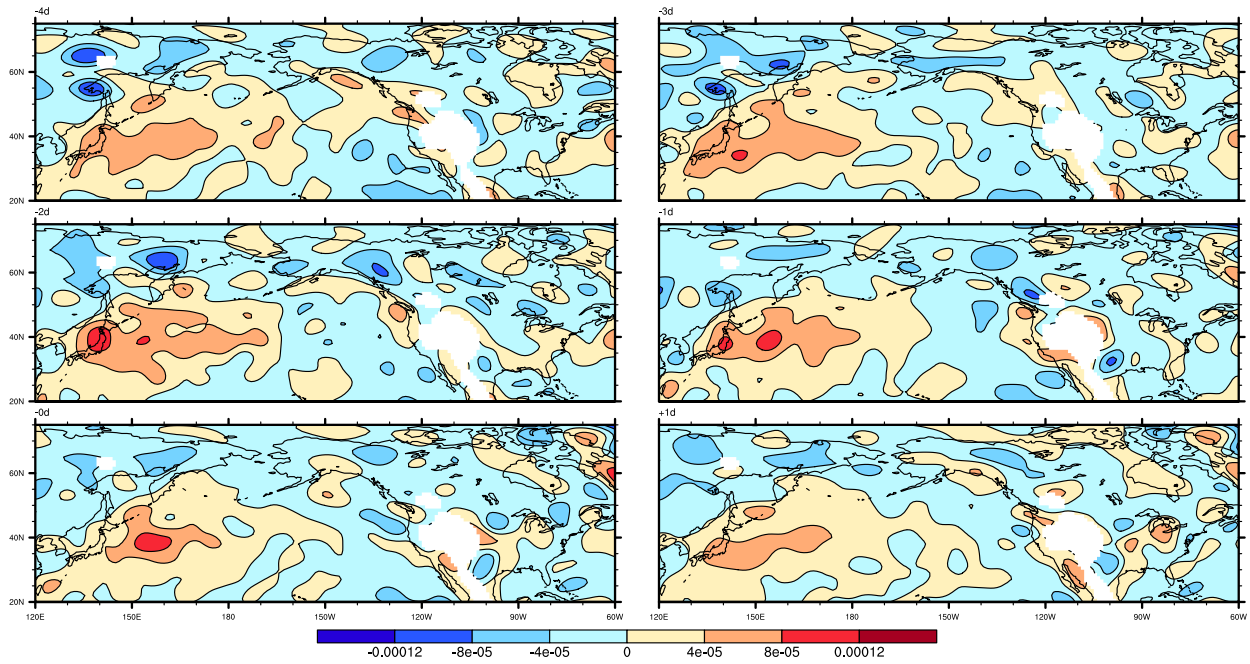


Fig 2 Same as figure 3.1.2, but for 850hPa. Regions with surface pressure lower than 850hPa are masked by white color.

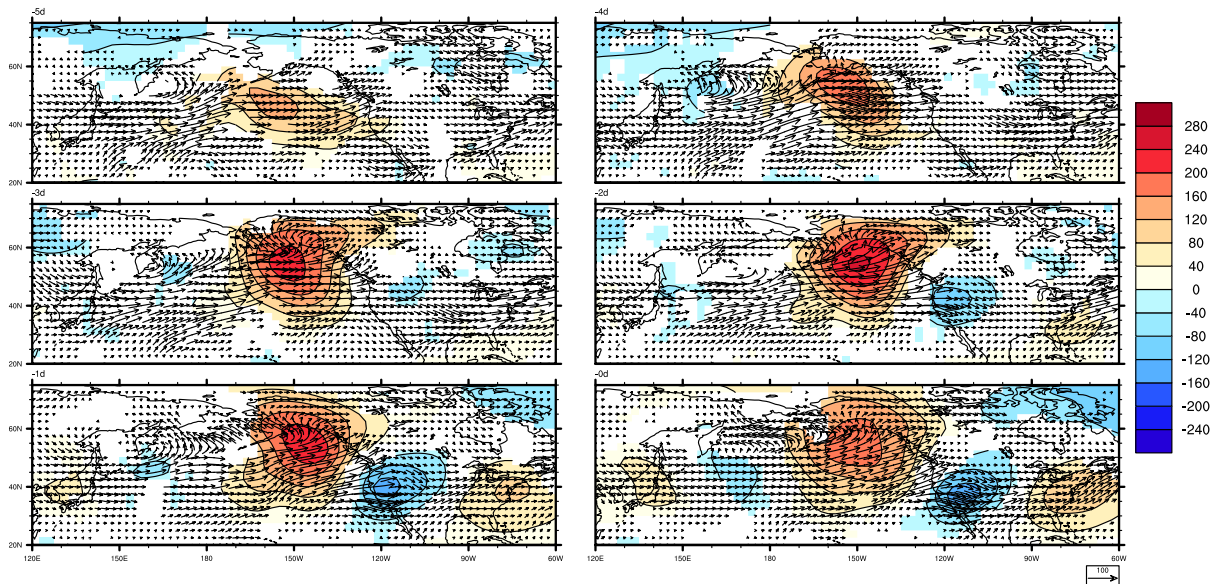


Fig 3 Same as figure 3.2.1 but for 700hPa.